A Method for Real-time Estimation of Full-scale Global Ice Loads on Floating Structures

Øivind K. Kjerstad[1,2] Wenjun Lu[1] Roger Skjetne[1, 2] Sveinung Løset[1]

[1]*Sustainable Arctic Marine and Coastal Technology (SAMCoT), Centre for Research-based Innovation (CRI)*

[2]*Dept. Marine Technology,*

Norwegian University of Science and Technology (NTNU), Trondheim, Norway

Contents

Abstract

This paper proposes an algorithm that uses conventional measurements found on-board ships coupled with additional inertial measurement units to estimate the motions and global loads acting on them. The work is motivated by the scarce availability of full-scale load data for sea-ice operations and by the invasive instrumentation of strain gauges used to obtain global loads of all degrees of freedom. Full-scale data are key to a number of design, operational, and research aspects related to sea-ice operations. The proposed algorithm is based on four Inertial Measurement Units (IMUs) that together with position and heading measurements are used to make estimates of dynamic linear and rotational acceleration (acceleration resulting in motion). We show how to use models updated with propulsion and wind measurements to estimate propulsion, hydrodynamic, wind, and ice loads through a setup catering to real-time implementation. A case study with the Swedish icebreaker Oden is presented and discussed. The algorithm effectively yields reasonable ice load history estimations and presents great potential in its further application to real-time global ice load estimations.

Keywords:

Global ice load; Inertial Measurement Units (IMUs); Accelerometers; Floating structure; Arctic Technology; Ocean Engineering.

1 Introduction

Sea-ice is found on roughly 10% of the world's ocean surface and mostly found in the Arctic and Antarctic Seas. It expands and melts under the influence of solar, atmospheric, oceanic, and tidal forcing where ice covers break up, open, and close as drifting ice floe fields (Leppäranta, 2011). Operating floating structures in such environments create several challenges related to interactions with ice. If they are not sufficiently investigated and incorporated into operation designs, resulting consequences may range from minor damages to devastation. Thus, a system that can accurately measure the load levels in real-time can provide important information that facilitates an improved understanding of ice loads and consequent risk control measures. Field data are of great value. With reliable ice loads measured in the field, traditional empirical ice load formulas (e.g., Lindqvist (1989) for level ice, Croasdale et al. (2009) for a broken ice field, and Dolgopolov et al. (1975) for ice ridge keel loads) can be evaluated/extended to unconventional structural forms or ice conditions. Moreover, newly developed ice load formulas (e.g., an ice floe's in-plane splitting (Lu et al., 2015a), out-of-plane failure (Lu et al., 2015b) or impact force (Timco, 2011)) can be thoroughly evaluated/adjusted. In particular, the successful measurement of field ice loads substantiates the development and validation of multi-purpose numerical models such as those described in the literature, e.g., (Lu et al., 2018; Lu et al., 2014; Lubbad et al., submitted in 2017; Lubbad et al., 2015; Metrikin et al., 2015; Sayed et al., 2015). It will also have broad applications to vessel and operation design, automatic motion control, and research.

To quantify the ice load experienced by a structure, one can resolve to direct ice load measurements or indirect calculations based on ice environment monitoring together with corresponding ice load models (ISO/FDIS/19906, 2010; Sanderson, 1988). When applying an indirect approach, difficulties arise when documenting and quantifying the neighbouring ice environment (Haas and Jochmann, 2003; Lu and Li, 2010; Lu et al., 2008; Lu et al., 2016b). Moreover, suitability issues and uncertainties affect various available ice load models for given ice conditions. In reference to direct field ice load measurements Palmer and Croasdale (2013) summarised the advantages and disadvantages of different existing measurement techniques. These techniques can be generally categorised into two groups, i.e., those measuring local ice loads based on strains or deflections, e.g., strain gauges, extensometers, ice load cells and panels, and those used to measure global ice loads, e.g., accelerometers and/or tilt meters. Theoretically speaking, when local measurement instrumentations are installed over the entire ice – structure interaction zones, the global ice load is merely a summation. However, this usually leads to practical and/or economic difficulties. For example, ice loads can be measured by installing strain gauges onto strategic hull-girder beams. Although this method is well established and a significant body of publications on this approach exists (see e.g. (ABS, 2011; Frederking, 2005; Lensu and Hänninen, 2003; Palmer and Croasdale, 2013; Ritch et al., 2008), the installation and calibration of strain gauges involves considerable effort and may in areas of the hull be difficult or impossible to execute. In this paper we investigate an alternative approach, i.e., estimating the global ice load from conventional measurements found on-board coupled with <u>four</u> additional inertial measurement units (IMUs). This option is particularly interesting, as installation of IMUs constitutes non-invasive and technologically mature instrumentation systems (Titterton and Weston, 2004) that enable sensing loads acting from any oblique angle. Achieving the same sensing capabilities with local instrumentations, e.g., strain gauges, involves extensive instrumentation around the entire hull. After obtaining the ship's inertia based on IMU measurements, well-established theoretical models are used to calculate other load components (hydrodynamic, propulsion and wind forces). Eventually, the ice load history can be indirectly calculated from these known load terms.

The IMU system to be introduced in this paper yields information such as linear accelerations in all three Degrees of Freedom (DoF) and angular rates in 3 DoF as well. Linear acceleration measurements are similar to those of former applications of accelerometers to ice engineering. However, improvements to previous accelerometer applications are made. For example, 1) in comparison to Danielewicz et al.'s (1983) method in which an ice floe's deceleration is measured to roughly back-calculate its impact load on a structure, the proposed algorithm uses all measured information, e.g., angular rates and ship Global Position System (GPS) information, to make accurate estimations on a ship's linear acceleration according to existing state estimator theories (Fossen, 2011f). In this way more accurate linear accelerations can be estimated for global load component calculations. 2) Compared to conventional accelerometer applications to ice induced vibration measurements, this paper focuses on a floating structure's responses according to IMU measurements. The relatively slower ship motion denotes that our interested data reside in a different frequency band; moreover, relatively significant ship motions, e.g., roll and pitch movements, introduce gravitational errors into accelerometer measurements that require further correction.

The idea of using IMUs for motion estimation is not new (Johnston et al., 2008a; Nyseth et al., 2013), and the results of Johnston et al. (2008b), wherein inertial measurements are compared to strain-gauges, are encouraging. This paper is novel in that it describes a system that estimates different load components based on available motion measurements, wind measurements, and propulsion measurements. The approach of modelling vessel propulsion, hydrodynamic, and wind loads is well established and fundamental to modern automatic motion control (e.g., dynamic positioning) (see e.g. (Fossen, 2011b; Sørensen, 2012)). However, such systems do not typically rely on acceleration measurements. Yet some exceptions exist (Kjerstad and Skjetne, 2016; Lindegaard, 2003). The benefits of the proposed algorithm are investigated based on a dataset from the Oden Arctic Technology Research Cruise in 2015 (OATRC2015), during which two Swedish icebreakers, the Oden and the Frej, conducted ice management (IM) trials amidst Arctic sea-ice north of Svalbard.

Fig. 1. The Swedish icebreakers Oden and Frej in Longyearbyen before OATRC2015 in September 2015. Courtesy Tomas Johansen.

2 Problem Formulation

In describing the 6-DoF motions of a rigid body marine surface vessel, we consider the following model,

$$\begin{aligned} \dot{\eta} &= J_{\Theta}(\eta)V \\ M\dot{V} &= \tau_p + \tau_h + \tau_w + \tau_i \quad , \end{aligned} \tag{1}$$

where $\eta = \mathrm{col}(P,\Theta) \in \mathbb{R}^6$ is the position $P = \mathrm{col}(x,y,z) \in \mathbb{R}^3$ and orientation $\Theta = \mathrm{col}(\phi,\theta,\psi) \in \mathbb{R}^3$ of the ship in the assumed-to-be-inertial North-East-Down (NED) frame. $V = \mathrm{col}(\upsilon,\omega) \in \mathbb{R}^6$ is the body-fixed linear $\upsilon = \mathrm{col}(u,v,w) \in \mathbb{R}^3$ and angular velocity $\omega = \mathrm{col}(p,q,r) \in \mathbb{R}^3$ of the body (see Fig. 2a), $M = M^{\mathrm{T}} > 0$ is the rigid-body inertia matrix, $\tau_p \in \mathbb{R}^6$ is the propulsion load, $\tau_h \in \mathbb{R}^6$ is the hydrodynamic load with drag and restoring forces, $\tau_w \in \mathbb{R}^6$ is the wind load, and $\tau_i \in \mathbb{R}^6$ is the ice load. The transformation matrix $J_\Theta(\eta) \in \mathbb{R}^{6\times 6}$ is given in (Fossen, 2011) as

$$J_\Theta(\eta) = \begin{bmatrix} R(\Theta) & 0 \\ 0 & T(\Theta) \end{bmatrix}, \tag{2}$$

Where $R(\Theta) \in SO(3)$ is the rotation matrix between the body frame and the NED frame, and $T(\Theta) \in \mathbb{R}^3$ is the angular velocity transformation matrix,

$$T(\Theta) = \begin{bmatrix} 1 & \sin(\phi)\tan(\theta) & \cos(\phi)\tan(\theta) \\ 0 & \cos(\phi) & -\sin(\phi) \\ 0 & \sin(\phi)/\cos(\theta) & \cos(\phi)/\cos(\theta) \end{bmatrix}. \tag{3}$$

Note that because Euler angles are used, $\theta = \pm\pi/2$ implies that two terms of Eq. (3) continue to infinity. However, for marine surface vessels this is not an issue, as $|\theta| \ll \pi/2$. When necessary, the singularities may be avoided by use of quaternion formulation.

Our main objective is to design an algorithm that is capable of determining η, V and $\dot{V}$ in addition to global loads τ_p, τ_h, τ_w and τ_i. It is assumed that the following time-synchronised signals are available for the algorithm:

1. A global navigation satellite system (GNSS) providing the vessel position P
2. A gyrocompass providing the vessel heading ψ.
3. Sensors in the propulsion system provide the individual rudder angle $\delta \in \mathbb{R}$, propeller pitch $\alpha_p \in \mathbb{R}$, and propeller rpm $n_p \in \mathbb{R}$.
4. Wind sensors provide the relative wind magnitude $U_{wind} \in \mathbb{R}$ and direction γ_{wind}.
5. Four IMUs, each provide measured linear accelerations at the sensor's mounting location, $a_m \in \mathbb{R}^3$, and at the measured angular velocity $\omega_m \in \mathbb{R}^3$.

With information from #1 and 2, in pursuit of η we are left with the to-be-calculated signal of ϕ roll and θ pitch angles; in pursuit of V, only the angular velocity ω is measured by the IMUs and we are left with estimations of the linear velocity υ; in pursuit of $\dot{V}$, only the linear acceleration a (to be introduced in Eq. (5)) can be derived from the IMUs' direct measurement, whereas the angular accelerations α (to be introduced in Eq. (5))

must be derived. With known ship acceleration information $\dot{V}$, the inertia force term $M\dot{V}$ in Eq. (1) is thus known. Furthermore, with the previously calculated linear velocity υ, and given the ship's geometry, the hydrodynamic force τ_h can be calculated as is described in Section 3.4. Provided with measurements in #3 and #4, the propulsion loads τ_p and wind force τ_w can be calculated as is described in Section 3.4. With these necessary terms estimated from physical models and measurements, the ice load τ_i can be calculated as the residual load from Eq. (1).

In the following we describe how to process the measurements from the IMUs, i.e., measured linear acceleration $a_m \in \mathbb{R}^3$ and measured angular velocity $\omega_m \in \mathbb{R}^3$, to exclude measurement noise and drift; we also transform spatially distributed measurements into the Common Origin (CO) of a ship.

An IMU is here referred to as a sensor containing a body-fixed three axis orthogonal linear accelerometer and a three-axis orthogonal gyroscope (see Fig. 2b).

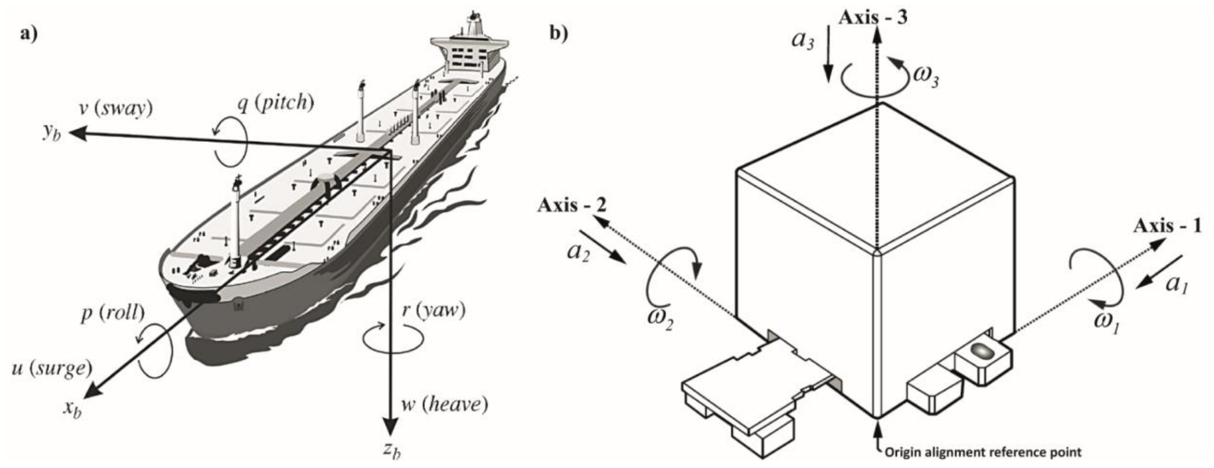

Fig. 2. a) The body-fixed coordinate system for a ship's motion (from Fossen (2011c)) and b) an example of an IMU's local measurement and corresponding coordinate system.

The IMU output is modelled as,

$$\begin{aligned}
a_m &= a_l - R(\Theta)^{\mathrm{T}} g_a + b_a + w_a \\
\dot{b}_a &= w_{ba} \\
\omega_m &= \omega + b_\omega + w_\omega \\
\dot{b}_\omega &= w_{b\omega} \quad ,
\end{aligned} \tag{4}$$

where a_m is the specific force measurement, $a_l \in \mathbb{R}^3$ is the linear dynamic acceleration of the sensor in its mounting point, ω_m and ω are measured and actual angular rate vectors, $g_a := \mathrm{col}(0,\, 0,\, g) \in \mathbb{R}^3$ is the gravitational vector, $b_a \in \mathbb{R}^3$ and $b_\omega \in \mathbb{R}^3$ are a slowly varying bounded biases, and where w_a, w_{ba}, w_ω, and $w_{b\omega} \in \mathbb{R}^3$ are zero mean white noise terms. The placement of the IMUs in the hull give rise to mounting dependence on the distance between the CO and the sensor mounting position, which is given by

$$a_l = a + \alpha \times l + \omega \times (\omega \times l) \tag{5},$$

where $a \in \mathbb{R}^3$ is the linear dynamic acceleration in CO, $\alpha \in \mathbb{R}^3$ is angular acceleration, and $l \in \mathbb{R}^3$ is the body frame distance vector between points of measurement and CO. The latter is referred to as the accelerometer lever arm or just as the lever arm. We note that $\dot{V} = \mathrm{col}(\upsilon, \omega) = \mathrm{col}(a, \alpha) \in \mathbb{R}^6$, which we are seeking. It is assumed that all measurements and parameters, except g_a, are decomposed in the body frame, after sensor calibration has been conducted.

The proposed algorithm is structured in Fig. 3 and described in Section 3. A case study of OATRC2015 based on the developed algorithm is presented in Section 4. In Section 5 we investigate the calculated results (the ship's motion results and various load components), and we particularly make necessary validations against the estimated ice load. Finally, conclusions are drawn in Section 6.

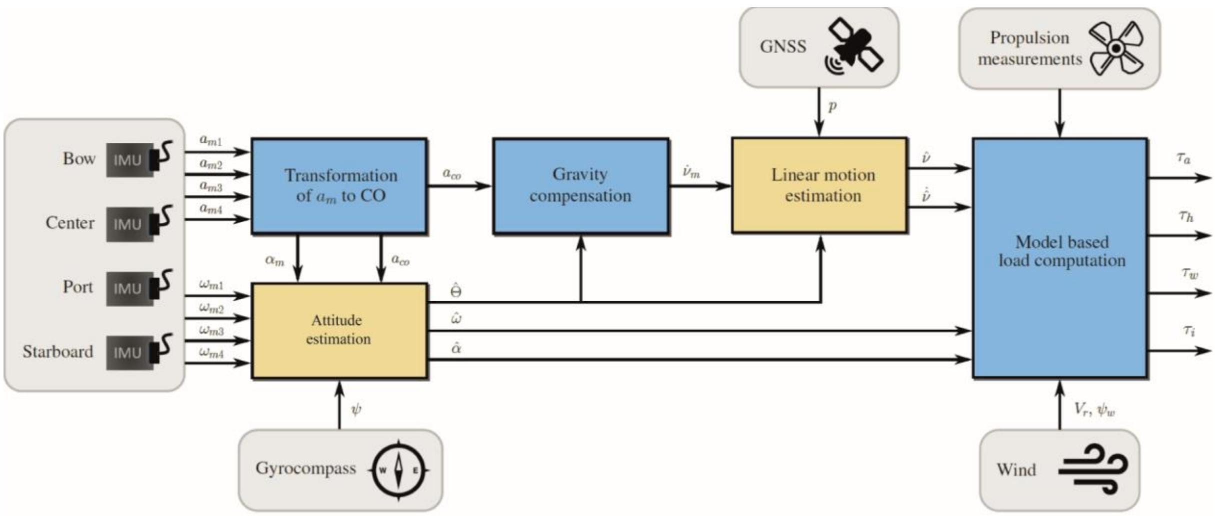

Fig. 3. Algorithm structure.

3 Algorithm Design

To overcome the challenges related to using accelerometers, we exploit four spatially distributed sensors and the relations between them. This enables the use of well known, matured, and relatively inexpensive conventional accelerometers in a spatial configuration to setup a virtual 6-DoF accelerometer in CO. Similar schemes are described in (Buhmann et al., 2006) and (Tan and Park, 2005). The other challenge of obtaining $\dot{V}$ is managed by reformulating the state observer. While the objective of this paper does not involve 6-DoF acceleration vector use in the ship's autopilot control algorithm (Kjerstad and Skjetne, 2016), it is practical to use an observer for the removal of gravity bias compensation, and noise filtering.

The next challenge is the fact that $a \in \mathbb{R}^3 \neq \dot{V} \in \mathbb{R}^6$. The dynamic acceleration a_l captured in an accelerometer (along with other effects) does not contain the angular acceleration α. It should be noted that sensors capable of measuring α exist (Titterton and Weston, 2004), but they are not commonly used in marine applications. Therefore, they are not considered here. We propose obtaining α by exploiting the lever arm dependencies of four distributed accelerometers. Thus, a third challenge involves acquiring $\dot{V}$ from these.

3.1 Transformation of acceleration measurements to CO

We parameterise Eq. (5) as a product of its static and dynamic variables

$$a_l = [I_{3\times3} \quad S(l)^{\mathrm{T}}{}_{3\times3} \quad H(l)_{3\times6}] \begin{bmatrix} a_{3\times1} \\ \alpha_{3\times1} \\ \varpi_{6\times1} \end{bmatrix} = W(l)_{3\times12} \begin{bmatrix} \dot{V}_{6\times1} \\ \varpi_{6\times1} \end{bmatrix} = W(l) z_{12\times1} \tag{6}$$

Where $I_{3\times3} \in \mathbb{R}^{3\times3}$ is the identity matrix, and $S(l)$ is given in Eq. (7) together with its properties,

$$S(l) = \begin{bmatrix} 0 & -l_z & l_y \\ l_z & 0 & -l_x \\ -l_y & l_x & 0 \end{bmatrix} = -S(l)^{\mathrm{T}}. \qquad (7),$$

The matrix

$$H(l) = \begin{bmatrix} 0 & -l_x & -l_x & l_y & l_z & 0 \\ -l_y & 0 & -l_y & l_x & 0 & l_z \\ -l_z & -l_z & 0 & 0 & l_x & l_y \end{bmatrix} \tag{8}$$

is a sub-matrix of the accelerometer configuration matrix $W(l) \in \mathbb{R}^{3\times12}$, and $z = \mathrm{col}(a, \alpha, \varpi) \in \mathbb{R}^{12}$ is the linear acceleration, angular acceleration, and angular rate cross product vector. The latter includes $\varpi \in \mathbb{R}^{6}$ defined as

$$\varpi = [\omega_x^2 \quad \omega_y^2 \quad \omega_z^2 \quad \omega_x\omega_y \quad \omega_x\omega_z \quad \omega_y\omega_z]^{\mathrm{T}}. \tag{9}$$

As noted above, by measuring from one location, $W(l)$ cannot be inverted to find z. Therefore, we use a configuration of four sensors as illustrated in Fig. 4 such that Eq. (6) can be extended to Eqs. (10) and (11).

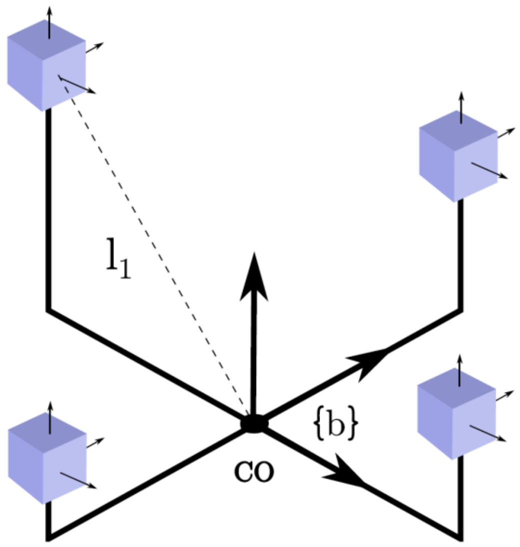

Fig. 4. Example of four IMU-based measurement system.

Note that in Fig. 4, the sensor frames of all the IMUs are alighted after calibration, which means that the respective linear acceleration measurements from all the IMUs, i.e., a_{m1}, a_{m2}, a_{m3}, and a_{m4}, are oriented in the same direction. Sensor misalignment is typically handled by calibration. Hence, no additional relative angle information among IMU orientations need to be taken into account in Eqs. (7) and (8). This stands in direct comparison to the IMU configuration developed by Buhmann et al. (2006), shown in their paper's Fig. 2, for which relative angles among different IMUs are accounted for in Buhmann et al.'s (2006) Eq. (4). When we set all angles of Eq. (4) developed by Buhmann et al. (2006) as zero, the components of $S(l)$ and $H(l)$ are obtained. This signifies the correctness of our formulations for Eqs. (7) and (8).

For the combined four-sensor inclusive formulation of Eqs. (10) and (11),

$$\begin{bmatrix} a_{l1} \\ a_{l2} \\ a_{l3} \\ a_{l4} \end{bmatrix}_{12\times 1} = \begin{bmatrix} W(l_1) \\ W(l_2) \\ W(l_3) \\ W(l_4) \end{bmatrix}_{12\times 12} z_{12\times 1} \tag{10}$$

$$a_{c\,12\times 1} = G(l_c)_{12\times 12}\, z_{12\times 1} \tag{11),$$

$a_c \in \mathbb{R}^{12}$ denotes the combined linear acceleration vectors at the sensor mounting positions, $G(l_c)$ is the combined sensor configuration matrix, and $l_c = \mathrm{col}(l_{c1} \quad l_{c2} \quad l_{c3} \quad l_{c4})$ is the combined sensor lever arm vector. To calculate z it is important to ensure that the static matrix $G(l_c)$ is nonsingular. According to Zappa et al. (2001), this is achieved when sensors are oriented equally and when their positions are not co-planar, that is at least one sensor must not lie in the same plane as the three others. Let $b = \mathrm{col}(b_1,\ b_2,\ b_3,\ b_4)$ and $w = \mathrm{col}(w_1 \ \ w_2 \ \ w_3 \ \ w_4)$. Then, by substituting the four accelerometer equations of Eq. (4) into the combined vector a_c we get

$$\begin{aligned} z &= G(l_c)^{-1}(a_{mc} + 1_4 \otimes R(\Theta)^{\mathrm{T}} g_a - b - w) \\ a &= B_a z = [I_{3\times3},\ 0_{3\times3},\ 0_{3\times6}]z \\ \alpha &= B_\alpha z = [0_{3\times3},\ I_{3\times3},\ 0_{3\times6}]z \end{aligned} \tag{12),$$

where $1_4 \in \mathbb{R}^4$ is a vector of ones, $\otimes$ is the Kronecker product, $a_{mc} = \mathrm{col}(a_{m1},\ a_{m2},\ a_{m3},\ a_{m4})$ is the specific force measurement of each of the four IMUs and B_a and B_α are selection matrices for the accelerations a and α within z. This shows that the setup with four spatially distributed accelerometers constitutes a 6-DoFs sensor placed in CO, yielding our target value $\dot{V}$ embedded within z. Note that it still has the same sensor effectsin terms of gravity, bias, noise as Eq. (4) does on the individual measurements.

However, in Eq. (12) the angular attitude $\Theta \in \mathbb{R}^{3\times3}$ of the ship, with the exception of the vessel's heading ψ are yet to be determined. Therefore, in processing the measured data a_{mc} we applied a two-step approach. In the first step, the intermediate variable z' is calculated according to Eq. (13) by transforming individual measurements into the CO, that is,

$$z' = G(l_c)^{-1} a_{mc} \tag{13}$$

for which we note that

$$a' = B_a z' = a - B_a G(l_c)^{-1}(1_4 \otimes R(\Theta)^{\mathrm{T}} g_a - b - w) \tag{14}$$

Since parameters a, b, and w are much smaller than the gravity acceleration g (in the vertical direction g_a) for a large icebreaker vessel, it follows from the last equation that a' is dominated by the gravity vector. Since this vector is decomposed in NED and, thus, points distinctly in the vertical direction towards the Earth centre, the roll and pitch angles can be deduced from this measurement a'. Hence, together with the gyrocompass yaw measurement ψ, the angular displacement $\Theta \in \mathbb{R}^{3\times 3}$ of the ship can be obtained, as further described in Section 3.2.

In the second step, given information of Θ, gravity compensation is further conducted in the second step at the CO following Eq. (15). Defining first the combined bias and noise vectors,

$$\begin{aligned} b_a &= B_a G(l_c)^{-1} b \\ w_a &= B_a G(l_c)^{-1} w \end{aligned}$$

and

$$\begin{aligned} b_\alpha &= B_\alpha G(l_c)^{-1} b \\ w_\alpha &= B_\alpha G(l_c)^{-1} w \end{aligned}$$

this gives the measured accelerations in CO,

$$\begin{aligned} a^m &= a' + B_a G(l_c)^{-1}(1_4 \otimes R(\Theta)^{\mathrm{T}} g_a) = a + b_a + w_a \\ \alpha^m &= B_\alpha z' + B_\alpha G(l_c)^{-1}(1_4 \otimes R(\Theta)^{\mathrm{T}} g_a) = a + b_\alpha + w_\alpha \end{aligned} \tag{15}$$

These measurement equations are next introduced to the Kalman filters described next.

3.2 Attitude estimation

Following the flow chart presented in Fig. 3, after obtaining the linear acceleration a_{mc} at four different mounting locations and its transformed information z at CO according to Eq. (12), we are facing with the estimation of roll angle ϕ and pitch angle θ within the orientation $\Theta = \mathrm{col}(\phi, \theta, \psi) \in \mathbb{R}^3$. There is no direct measurement of these two variables. However, as mentioned above, they can be derived from two sources.

First, by assuming that the average acceleration with respect to the environment is zero and much less than the vertical gravity component of g_a (Noureldin et al., 2012), the roll and pitch angle can be calculated from $a' = \mathrm{col}(a_x^{'}, a_y^{'}.a_z^{'})$ following Eqs. (16) and (17) , that is,

$$\phi_m \approx \mathrm{atan2}(-a_y^{'}, -a_z^{'}) \quad \rightarrow \text{roll angle} \tag{16}$$

$$\theta_m \approx \mathrm{atan2}(a_x^{'}, \sqrt{(a_y^{'})^2 + (a_z^{'})^2}) \quad \rightarrow \text{pitch angle} \tag{17},$$

in which $\mathrm{atan2}(\cdot,\cdot)$ is used to robustly calculate $\mathrm{atan}(\cdot)$ with correct quadrant mapping of the angles in $[-\pi, \pi)$. The above calculation suffers from noise in the IMU acceleration measurements. Moreover, short-term vibrations and external forces that directly influence the linear accelerations and nonlinear equations in Eqs. (16) and (17) will further magnify these disturbances. Therefore, the calculated roll and pitch angles from the linear accelerations' measurement are denoted as ϕ_m and θ_m, respectively.

Second, angular rates $\omega = \mathrm{col}(p, q, r) \in \mathbb{R}^3$ are directly measured by the installed IMUs. We adopt the kinematic model in Eq. (18), in which the orientation rate $\dot{\Theta}$ can be transformed from the body-fixed angular velocity $\omega = \mathrm{col}(p, q, r) \in \mathbb{R}^3$.

$$\dot{\Theta} = T(\Theta)\omega \tag{18},$$

and in Eq. (19) the angular acceleration α is related to $\dot{\omega}$.

$$\dot{\omega} = \alpha \tag{19},$$

Ideally, integrating $\dot{\Theta}$ once gives us Θ, which includes the roll ϕ and pitch angles θ. This approach removes short-term noise but spurs long-term drift due to accumulated integration errors. In this paper we use the Unscented Kalman Filter (UKF) (Julier and Uhlmann, 2004) to take advantage of the angular information obtained from both the measurements described in Eqs. (16) and (17); and the integration procedures described in Eqs. (20) to (24) based on Eqs. (18) and (19).

In Eqs. (20) and (21) below, Δ denotes the time step between two consecutive angular rate estimations. A hat symbol '^' is introduced to the rotation rate to differentiate between the estimated state value and its corresponding true value. Each predictive step according to the physical model in Eqs. (18) to (24) is updated/corrected according to corresponding measurements presented in Eqs. (16) and (17) following the standard UKF algorithms and forward Euler integration, that is,

$$\hat{\Theta}_{k+1} = \hat{\Theta}_k + \Delta T(\hat{\Theta}_k)\hat{\omega}_k \tag{20}$$

$$\hat{\omega}_{k+1} = \hat{\omega}_k + \Delta\hat{\alpha}_k \tag{21}$$

$$\hat{\alpha}_{k+1} = \hat{\alpha}_k \tag{22}$$

$$\hat{b}_{\omega,k+1} = \hat{b}_{\omega,k} \tag{23}$$

$$\hat{b}_{\alpha,k+1} = \hat{b}_{\alpha,k} \tag{24}$$

3.3 Linear motion estimation

In the NED system, the ship's position $P_m = \mathrm{col}(x_m, y_m, z_m) \in \mathbb{R}^3$ can be calculated from logged GPS data. The ship velocity can be derived from Eq. (25) by simply making a time derivative of the position data. Similarly, a subscript '*m*' is introduced to signify their connections to the measurement procedure under the UKF framework.

$$\dot{P}_m = \mathrm{col}(\dot{x}_m, \dot{y}_m, \dot{z}_m) = \mathrm{col}(v_{Nm}, v_{Em}, v_{Dm}) \tag{25}$$

On the other hand, a kinematic relationship can be established from the acceleration vector a obtained from the spatially distributed IMU setup. This is expressed as Eqs. (26) and (27).

$$\dot{P} = R(\Theta)\upsilon \tag{26}$$

$$\dot{\upsilon} = a \tag{27}$$

In this study, the same UKF scheme is used to exploit linear motions (i.e., both the position and velocity in the NED system and acceleration in the body-fixed system) from two different sources (i.e., GPS and IMU measurements). A similar forward Euler integration scheme is used in Eqs. (28) to (30) as the physical system to estimate the ship's linear motion. This predictive step in the UKF is corrected by measured information in Eq. (25) following standard UKF procedures.

$$\hat{p}_{k+1} = \hat{p}_k + \Delta R(\hat{\Theta}_k)\hat{v}_k \tag{28}$$

$$\hat{v}_{k+1} = \hat{v}_k + \Delta a_k \tag{29}$$

$$\hat{b}_{a,k+1} = \hat{b}_{a,k} \tag{30}$$

Note, however, that the linear acceleration term at the CO in Eqs. (27) and (29) is not the same as that calculated based on Eq. (12). Following from Section 3.2, relatively accurate roll $\hat{\phi}_k$, pitch $\hat{\theta}_k$ and yaw angles $\hat{\psi}_k$ in the NED system have been estimated. Before we proceed to estimate the ship's linear motion in Eqs. (28) to (30), as shown in the algorithm in Fig. 3, it is necessary to simultaneously execute gravity compensation following Eq. (15) using updated rotational matrix from Eqs. (31) to (32) to obtain the updated linear acceleration a_k of each time step.

$$\hat{R}_{x,\phi} = \begin{bmatrix} 1 & 0 & 0 \\ 0 & \cos\hat{\phi}_k & -\sin\hat{\phi}_k \\ 0 & \sin\hat{\phi}_k & \cos\hat{\phi}_k \end{bmatrix},\ \hat{R}_{y,\theta} = \begin{bmatrix} \cos\hat{\theta}_k & 0 & \sin\hat{\theta}_k \\ 0 & 0 & 0 \\ -\sin\hat{\theta}_k & 0 & \cos\hat{\theta}_k \end{bmatrix},\ \hat{R}_{z,\theta} = \begin{bmatrix} \cos\hat{\psi}_k & -\sin\hat{\psi}_k & 0 \\ \sin\hat{\psi}_k & \cos\hat{\psi}_k & 0 \\ 0 & 0 & 1 \end{bmatrix} \tag{31}$$

$$\hat{R} = \hat{R}_{z,\theta}\hat{R}_{y,\theta}\hat{R}_{x,\phi} \tag{32}$$

3.4 Load component calculation

With the algorithms implemented in the previous sections, ship motions in both the NED and body-fixed systems are available in all 6 DoFs. Similarly, all load components can be formulated in 6 DoFs from known environmental, structural, and machinery data (i.e., wind, current, ship speed, propeller and rudder information). The load components' formulation relies on the use of well-established methods and its complete formulation in all 6 DoFs brings little novelty to this paper. For exemplary purposes and in response to our selected case study (i.e., ship transit in ice), our load components are formulated only for 3 DoFs in the surge, sway and yaw directions. In the following the formulation of each load component is described with the icebreaker Oden as an example.

- Inertia term $M\dot{V}$

Within the inertia term, acceleration in the surge, sway and yaw directions is estimated based on the previously introduced state estimator. The mass matrix M includes both the mass of the floating body and its added mass effect. In the case study described below we use 110% and 200% of the ship's mass in the surge and sway directions, respectively, to construct mass matrix M as an approximation according to relevant studies performed on ship structures (Faltinsen, 1993).

- Ship propulsion τ_p

For ship propulsion τ_p, two different components are calculated in the developed algorithm, i.e., propeller thrusting T_p according to Eq. (34) and the rudder's lift and drag forces according to Eq. (35). Detailed calculation procedures used to attain each of the following parameters can be found in other literatures (e.g., (Molland et al., 2017; Perez, 2006)).

$$T_p = \rho_w D^4 K_T |n| n \tag{33}$$

$$\begin{aligned} D_r &= \frac{1}{2}\rho_w A_f C_{Dr} u_r^2 \\ L_r &= -\frac{1}{2}\rho_w A_f C_{Lr} u_r^2 \end{aligned} \tag{34}$$

in which

n	describes the rotational speed of the propeller in 'revolutions per second [RPS]'. During transit, the time history of n is logged separately for the Starboard and Port side propellers;
D	is the diameter of Oden's propeller, $D = 4.8\,\mathrm{m}$;
D_r and L_r	is the drag and lift force acting on the rudder due to passing fluid (see Fig. 5);
K_T	is the thrust coefficient, which is calculated as shown in, e.g., (Molland et al., 2017);
A_f	is the foil area of the rudder; and it is $A_f = 28\,\mathrm{m}^2$ for Oden;
C_{Dr} and C_{Lr}	are the drag and lift coefficients for the rudder. Corresponding calculations are given in, e.g., Perez (2006);
u_r	is the flow velocity across the rudder and its calculation is given by, e.g., Perez (2006).

With the calculated force component history, propulsion can be formulated as shown in Eq. (36),

$$\tau_p = \begin{bmatrix} T_{p\_s} + T_{p\_p} - D_{r\_s} - D_{r\_p} \\ L_{r\_s} + L_{r\_p} \\ -\mathrm{LCG} \cdot (L_{r\_s} + L_{r\_p}) + \mathrm{TCG} \cdot (-T_{p\_s} + T_{p\_p}) \end{bmatrix} \begin{matrix} \rightarrow \text{surge} \\ \rightarrow \text{sway} \\ \rightarrow yaw \end{matrix} \tag{35}$$

in which the propeller thruster T_p is further distinguished as thrust from the Starboard side T_{p_s} and Port side T_{p_p}. The same convention applies to Starboard and Port side rudder drag and lift forces with additional subscripts –*s* and –*p*. Additionally, the distance between the rudder and the Longitudinal Centre of Gravity LCG is 46 m, and the distance between the rudder and the Transverse Centre of Gravity TCG is 2.9 m. Definitions of these load components together with the action point and arms (i.e., LCG and TCG) are illustrated in Fig. 5.

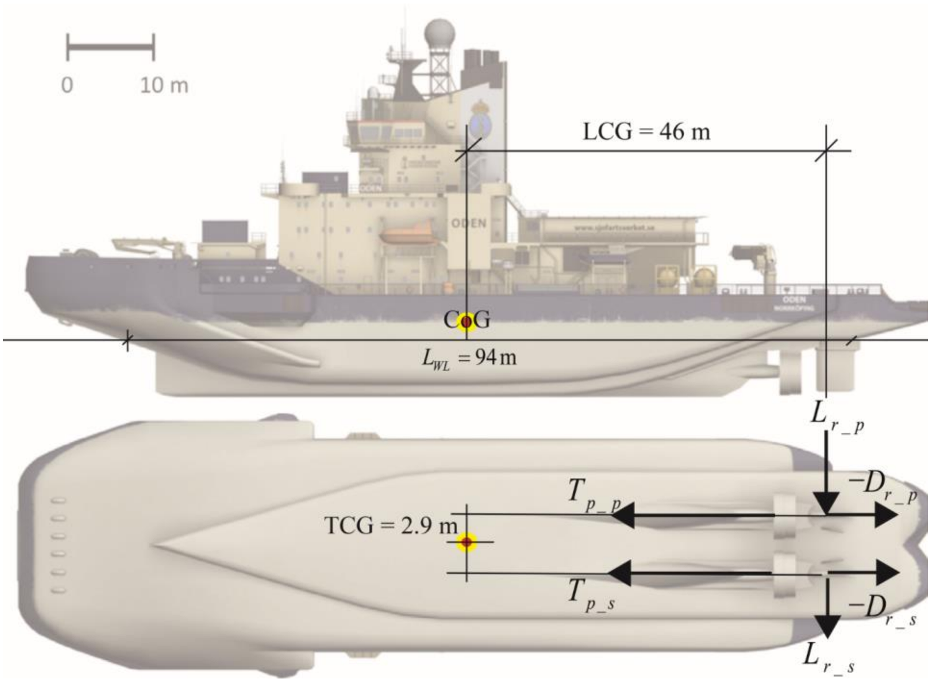

Fig. 5. Propulsion and rudder resistance for Oden (background images of Oden were developed by Tsarau et al. (2014)).

- Hydrodynamic force τ_h

The hydrodynamic force is formulated as shown in Eq. (37) according to Eq. (6.24) from Faltinsen (1993) for the surge direction, and Eqs. (7.98) and (7.99) from Fossen (2011e) are used for the sway and yaw directions. In addition, linear damping terms are included in Eq. (37). Linear viscous damping coefficients X_u, Y_v, and N_r can be calculated following Eqs. (6.76) to (6.81) described in Fossen (2011d).

$$
\begin{aligned}
&U_{total} = \sqrt{u^2 + v^2} \\
&\gamma = -\mathrm{atan2}(v, u) \\
&\tau_h = \begin{bmatrix} 1/2 \cdot \rho_w S(1+k) \dfrac{0.075}{(\log_{10} \mathrm{R_n} - 2)^2} |u| u + X_u u \\ 1/2 \cdot \rho_w A_Y C_{DY} U_{total}^2 + Y_v v \\ 1/2 \cdot L_{oa} \rho_w A_Y C_{DZ} U_{total}^2 + N_r \dot{\psi} \end{bmatrix} \begin{matrix} \rightarrow \mathrm{surge} \\ \rightarrow \mathrm{sway} \\ \rightarrow yaw \end{matrix}
\end{aligned}
\tag{36}
$$

In Eq.(36) U_{total} is the combined relative velocity of both surge and sway directions. Its components u (in surge) and v (in sway) are described in Section 3.3 via linear motion estimation; S is the wetted area of Oden; $k = 0.1$ is a coefficient for ship transit; $\mathrm{R_n} = uL_{WL} / v$ is the Reynolds number; $L_{WL} = 94\,\mathrm{m}$ is the length of the ship at the waterline; $v = 10^{-6}$ is the kinematic viscosity of water; $A_Y = 942.8\,\mathrm{m}^2$ is Oden's underwater projected area in the sway direction; $C_{DY} = 0.6\sin(\gamma)|\sin(\gamma)|$, $C_{DZ} = 0.1\sin(2\gamma)$ according to Figure 7.6 from Fossen (2011e); γ is the angle of encounter of the fluid relative to the bow for the ship during transit; and $L_{oa} = 108\,\mathrm{m}$ is the overall length of the ship.

- Wind drag τ_w

The wind drag is formulated in Eq.(38) according to Eqs. (8.20) to (8.23) from Fossen (2011a).

$$
\tau_w = 1/2 \cdot \rho_{air} \begin{bmatrix} A_X^{wind} C_{WX} U_{wind}^2 \\ A_Y^{wind} C_{WY} U_{wind}^2 \\ L_{oa} A_Y^{wind} C_{WZ} U_{wind}^2 \end{bmatrix} \begin{matrix} \rightarrow \mathrm{surge} \\ \rightarrow \mathrm{sway} \\ \rightarrow yaw \end{matrix}
\tag{37}
$$

with

$$
\begin{aligned}
C_{WX} &= -0.8\cos(\gamma_{wind}) \\
C_{WY} &= 0.8\sin(\gamma_{wind}) \\
C_{WZ} &= 0.1\sin(2\gamma_{wind})
\end{aligned}
\tag{38}
$$

In Eqs. (37) and (38), the wind speed U_{wind} and direction γ_{wind} are continuously logged during transit. $A_X^{wind} = 750\,\mathrm{m}^2$ and $A_Y^{wind} = 1250\,\mathrm{m}^2$ are Oden's above-water projected areas in the surge and sway directions, respectively.

4 Case Studies

The previously introduced algorithm can be applied to extract different load components' histories (particularly ice load histories) during a floating structure's operation/transit in ice. In this paper, the icebreaker Oden was chosen as the floating structure examined in our case studies.

4.1 Case description

As noted in the introduction, in September of 2015 a 14-day research expedition, OATRC2015, was carried out north of Svalbard. It was a two-ship operation involving the Swedish icebreakers Oden and Frej (shown in Fig. 1) for the study of Ice Management (IM) and ship performance in ice. Both icebreakers were heavily instrumented for various scientific purposes. For the case study presented in this paper we are interested in reconstructing all physical terms in Eq. (1) from the available data and physical models described. Among a great amount of research activities during OATRC2015, we examine a case featuring Oden's transit in marginal ice zone.

More specifically, on September 30th, 2015, after completing all research activities, the fleet started its return voyage. Approximately 6 hours before Oden started her return journey at 06:00:00, the helicopter aboard Oden was sent out to map ice conditions in the marginal ice zone, into which Oden shall transit through. The helicopter's flight route above ground is illustrated in Fig. 6 together with sampled images taken from the helicopter, illustrating the corresponding ice conditions. The flight had the purpose of characterising the ice across the ice edge and partly along it. The flight headed south towards the edge and then turned west at the edge before returning north to Oden. After the helicopter's photo mission, Oden was in drifting mode from 00:00:05 on September 30th until she started transit. Oden's path and the helicopter route above ground are illustrated in Fig. 7. In addition, from Oden's drift information we can plot the estimated 'helicopter's flying route' above the ice after taking into account ice drift corrections. We can see that for the time window of 06:49:00 to 07:35:00 there is an overlap between Oden's path and ice conditions filmed along the helicopter route.

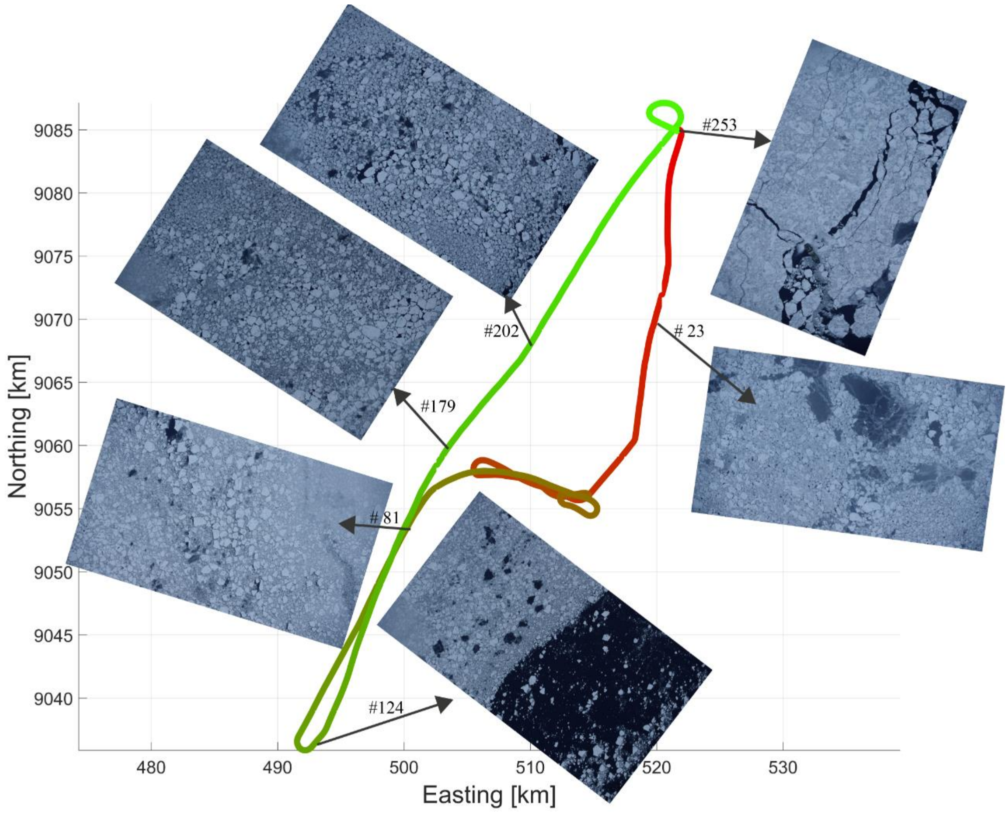

Fig. 6. Helicopter's flight route (from red to green) together with sample photos of ice conditions.

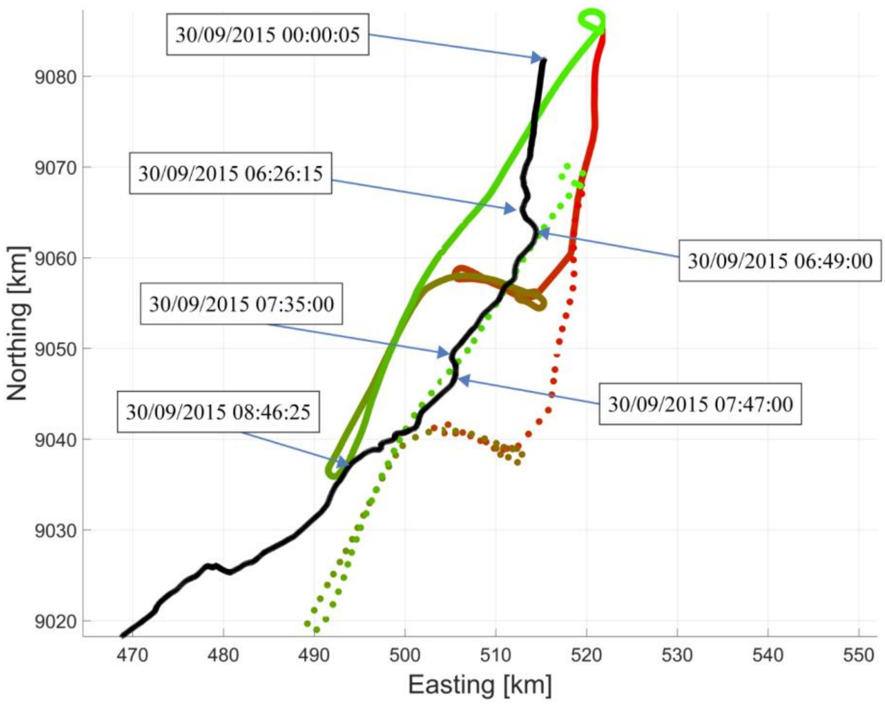

Fig. 7. Oden's path (dotted line running north to south); helicopter’s flight route above ground (solid coloured line from red to green); and the estimated flight route with ice drift corrections (dotted coloured line from red to green).

Such detailed documentation of ice conditions allows us to study the developed algorithm to make a real-time estimate of the global ice load acting on floating structures in this paper.

4.2 Setup and data logging

In accordance with the algorithm design, four IMUs were installed at different areas of Oden during the selected transit time window. Fig. 8 shows the approximate locations of the non-coplanar IMUs. Relevant sensor locations for the case studies, e.g., GPS, wind data and propeller information are also illustrated in Fig. 8. Specifically, for the calculations of $S(l)$ and $H(l)$ using Eqs. (7) and (8), the lever arm of each IMU is measured during installation as shown in Table 1.

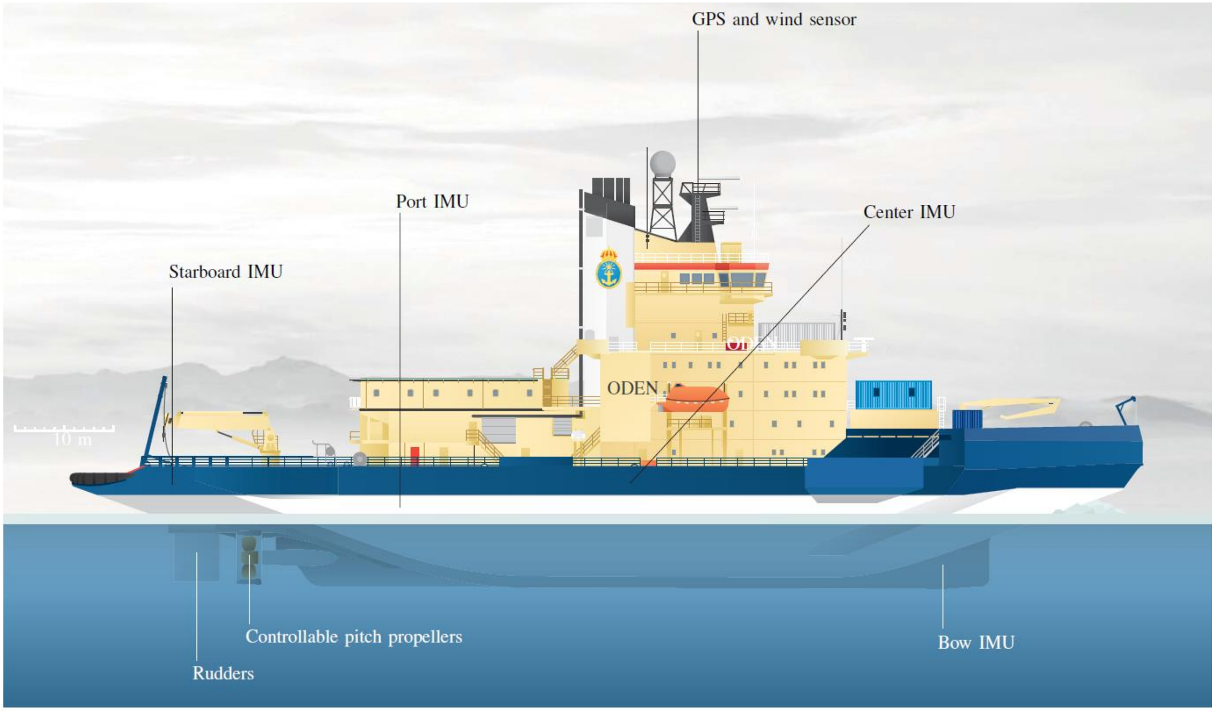

Fig. 8. Approximate locations of the four installed IMUs, GPS, wind sensor and propeller.

Table 1. Lever arm length of each IMU.

IMU #	Location	l_x [m]	l_y [m]	l_z [m]
1	CG	1.60	0.97	-0.6
2	Bow	33	-1.25	5
3	Port	-15.2	-10	7
4	Starboard	-47.81	3.975	1

4.2.1 <u>Calibration of raw IMU measurements</u>

The parameterisation of $S(l)$ and $H(l)$ in Eqs. (7) and (8) requires that all four IMUs' linear acceleration measurements are in line with one another as shown in Fig. 4. However, during IMU installation it was difficult to ensure that all IMUs were perfectly aligned, potentially for various practical reasons, e.g., imperfectly flat surface on which the IMU was attached (see Fig. 9). Therefore, before we use data directly measured from the IMUs and feed it to a_{mc} in Eq. (13), an initial calibration of raw measurements $a'_{mc} = \mathrm{col}(a'_{m1};\ a'_{m2};\ a'_{m3};\ a'_{m4})_{12\times1}$ is carried out to ensure that all IMUs are optimally aligned.

As installation imperfections were rather limited (in the range of 3^{o}), calibration was carried out using a numerical search algorithm. Calibration was carried out over two consecutive steps. First, corrections in the roll and pitch directions were separately made for each individual IMU, and then a correction in the yaw direction for all IMUs was conducted with reference to IMU #1. Our methods and calibration results are described in the following section.

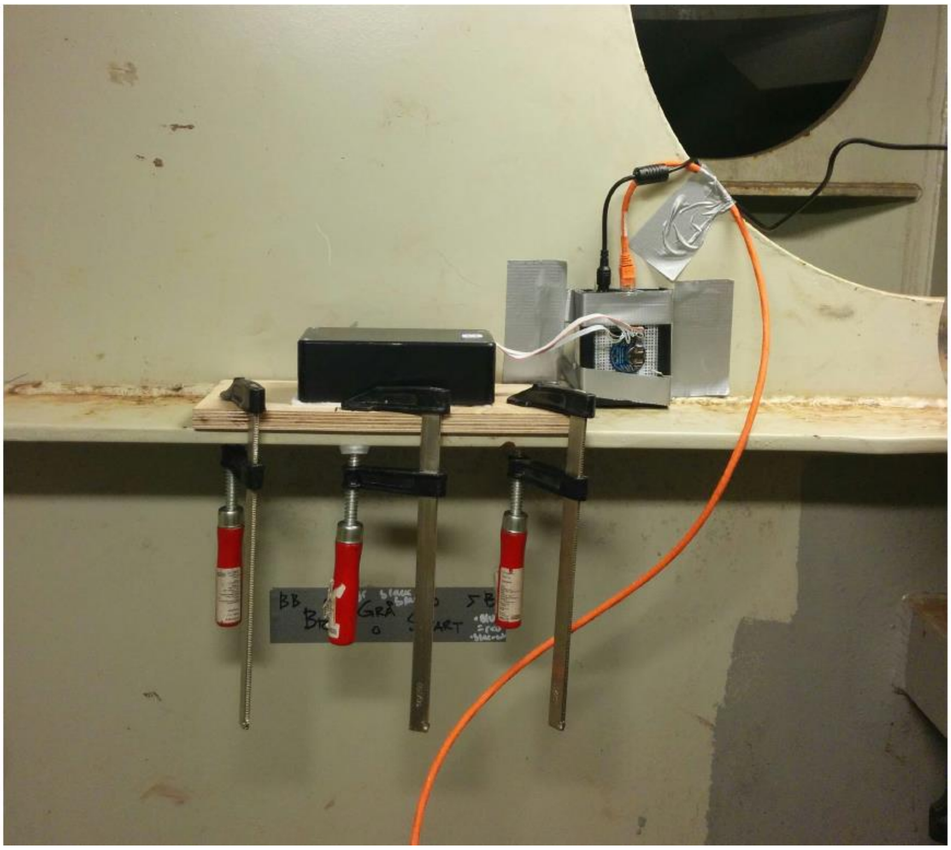

Fig. 9. Installation of the IMUs aboard Oden.

- Corrections made in the roll and pitch directions

Suppose a ship is standing still in calm water. When an IMU is perfectly installed on board with all of its axes in line with the ship's box-fixed coordinate system (i.e., all three axes for the ship and IMU are perfectly aligned in their respective directions as shown in Fig. 2), its linear acceleration measurement in the vertical direction should be g. However, when an IMU is installed with initial errors in the pitch and/or roll directions, the IMU's vertical axis (e.g., axis-3 in Fig. 2) is not in line with the gravitational pull or with the vertical axis z_b as shown in Fig. 2. This means that the IMU's raw linear acceleration measurement in the vertical direction $a_z^{'}$ should be smaller than g_a.

For our case study, the ship is constantly in motion. Intuitively we allow for the measured raw liner accelerations in all three directions for each IMU a'_{mi} $(i=1,2,3,4)$ to rotate in the roll and pitch directions within a certain range; and a numerical search is conducted within this range for each IMU to determine the optimal combination of roll and pitch corrections such that it yields the largest vertical component of the measured linear accelerations. For IMU #*i*, the procedure is to look for the roll and pitch adjustment $\Delta\Theta$, that a new linear acceleration vector at time '*k*' can be calculated as in Eq. (40). Afterwards, the time history of the linear acceleration $a_{mi,z,k}$ in the vertical direction is averaged in accordance with Eq. (41). The value of $\bar{a}_{mi,z}$ is to be maximized by varying $\Delta\phi$ and $\Delta\theta$.

$$\begin{gathered}\begin{bmatrix}\phi_i^{adjusted}\\ \theta_i^{adjusted}\\ \psi_i^{adjusted}\end{bmatrix}=\begin{bmatrix}\phi_i^{installation}\\ \theta_i^{installation}\\ \psi_i^{installation}\end{bmatrix}+\begin{bmatrix}\Delta\phi_i\\ \Delta\theta_i\\ 0\end{bmatrix},\qquad i=1,2,3,4,\quad \text{and}\ \ \psi_i^{adjusted}=90^{\circ}\ \ \text{when}\ \ i=1\\ \begin{bmatrix}a_{mi,x,k}\\ a_{mi,y,k}\\ a_{mi,z,k}\end{bmatrix}=R(\Theta^{adjusted})\begin{bmatrix}a'_{mi,x,k}\\ a'_{mi,y,k}\\ a'_{mi,z,k}\end{bmatrix},\qquad \Theta^{adjusted}=\begin{bmatrix}\phi_i^{adjusted}\\ \theta_i^{adjusted}\\ \psi_i^{installation}\end{bmatrix}\end{gathered}\tag{39}$$

$$\bar{a}_{mi,z}=\sum_{k=1}^{N}\left|a_{mi,z,k}\right|/N\tag{40}$$

Fig. 10 presents the results of the search algorithm. The adjustment made in the roll and pitch directions corresponds to the combination of $\phi^{adjusted}$ and $\theta^{adjusted}$, rendering it the largest vertical component of the averaged linear acceleration measurement. The search algorithm has an accuracy level of 0.05°, ensuring the accurate alignment of all four IMUs in the roll and pitch directions.

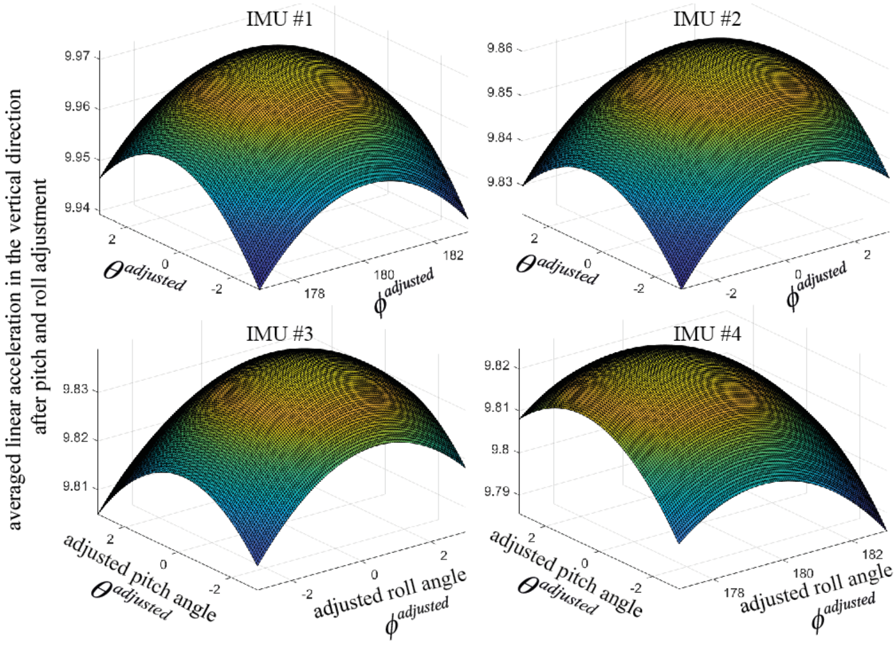

Fig. 10. Roll and pitch corrections made by searching for the adjustment combination yielding largest linear acceleration measurement of the vertical direction.

- Correction made in the yaw direction

For the correction made in the yaw direction, a reference measurement, i.e., IMU #1, is chosen. The idea is that after an adjustment of $\Delta\psi$ is made to the yaw angle, an IMU's angular velocity measurements $\omega_{mi} = \mathrm{col}(p_{mi}, q_{mi}, r_{mi})$ of the x_b, y_b, and z_b directions should have the lowest covariance in reference to the corresponding measurement from IMU #1. At a time instant 'k', the new angular velocity is calculated from Eq. (42) after a trial adjustment is made in yaw direction, i.e., $\Delta\psi$. $\phi^{adjusted}$ and $\theta^{adjusted}$ were identified from the previous step.

$$\begin{gathered}\begin{bmatrix}\phi_i^{adjusted}\\ \theta_i^{adjusted}\\ \psi_i^{adjusted}\end{bmatrix} = \begin{bmatrix}\phi_i^{adjusted}\\ \theta_i^{adjusted}\\ \psi_i^{installation}\end{bmatrix} + \begin{bmatrix}0\\ 0\\ \Delta\psi_i\end{bmatrix}, \quad i = 1,2,3,4, \quad \text{and} \quad \psi_i^{adjusted} = 90^\circ \ \text{when} \ i = 1 \\ \begin{bmatrix}p_{mi,x,k}\\ q_{mi,y,k}\\ r_{mi,z,k}\end{bmatrix} = R(\Theta^{adjusted})\begin{bmatrix}p'_{mi,x,k}\\ q'_{mi,y,k}\\ r'_{mi,z,k}\end{bmatrix}, \quad \Theta^{adjusted} = \begin{bmatrix}\phi_i^{adjusted}\\ \theta_i^{adjusted}\\ \psi_i^{adjusted}\end{bmatrix}\end{gathered} \tag{41}$$

Then, Eqs. (43) and (44) are introduced to quantify the error between the above adjusted angular velocity in reference to IMU #1's measurements. The goal is to minimise the error by varying $\psi^{adjusted}$. Fig. 11 illustrates the numerical search for yaw angles and the outcomes of corresponding minimal errors.

$$E = \begin{bmatrix} p_{mi,x,k} - \sum_{k=1}^{N} p_{mi,x,k} / N \\ q_{mi,y,k} - \sum_{k=1}^{N} q_{mi,y,k} / N \\ r_{mi,z,k} - \sum_{k=1}^{N} r_{mi,z,k} / N \end{bmatrix} - \begin{bmatrix} p_{m1,x,k} - \sum_{k=1}^{N} p_{m1,x,k} / N \\ q_{m1,y,k} - \sum_{k=1}^{N} q_{m1,y,k} / N \\ r_{mi,z,k} - \sum_{k=1}^{N} r_{mi,z,k} / N \end{bmatrix} \tag{42}$$

$$\text{A measure of error} = E^{\mathrm{T}} \cdot E \tag{43}$$

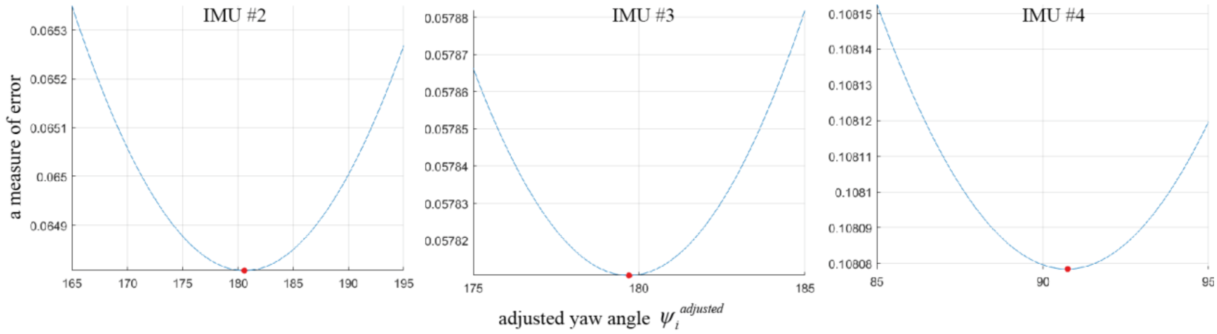

Fig. 11. Yaw corrections made by searching for the adjustment yielding the lowest error in angular rates with reference to IMU #1's measurements.

Table 2 summarised the adjusted installation angle. Evidently, a rather small adjustment is needed to ensure our previous search criteria. This implies a rather accurate installation in terms of the IMUs' initial orientation. Nevertheless, after the performed calibration, the updated IMU measurement can be used for further calculations from Eq. (13).

Table 2. Aligning all IMUs by adjusting installation angles of the roll, pitch and yaw directions in [deg].

IMU #	$\phi_i^{installation}$	$\phi_i^{adjusted}$	$\Delta\phi_i$	$\theta_i^{installation}$	$\theta_i^{adjusted}$	$\Delta\theta_i$	$\psi_i^{installation}$	$\psi_i^{adjusted}$	$\Delta\psi_i$
1	180.00	180.40	0.40	0.00	-0.15	-0.15	90.00	90.00	0.00
2	0.00	0.35	0.35	0.00	-0.65	-0.65	180.00	180.60	0.60
3	0.00	-0.30	-0.30	0.00	-0.45	-0.45	180.00	179.70	-0.30
4	180.00	180.65	0.65	0.00	0.60	0.60	90.00	90.75	0.75

5 Results and discussion

With all the required data (described in Section 2) collected, the designed algorithm are used to estimate the ship's movements and associated load components. In this section the results of the designed algorithm for Oden's MIZ transit case are presented together with a discussion.

5.1 Attitude estimation

Euler angle results for the selected time window are presented in Fig. 12. Both the 'measured data' by Eqs. (16) and (17) and the calculated results based on state 'estimations' are presented. As is shown in Section 3.3, Eqs. (16) and (17)'s calculations are susceptible to short-term noise and error magnifications due to the use of the nonlinear 'atan' function. This is reflected in Fig. 12, in which a relatively larger scatter of ϕ roll and θ pitch history can be found in the 'measurements'. After combining information collected from angular velocity measurements with the formulated physical process (see Section 3.3), the estimated Euler angle is alleviated from short-term noise and long-term drift. This eventually yields a more accurate Euler angle history for forthcoming linear acceleration calculations.

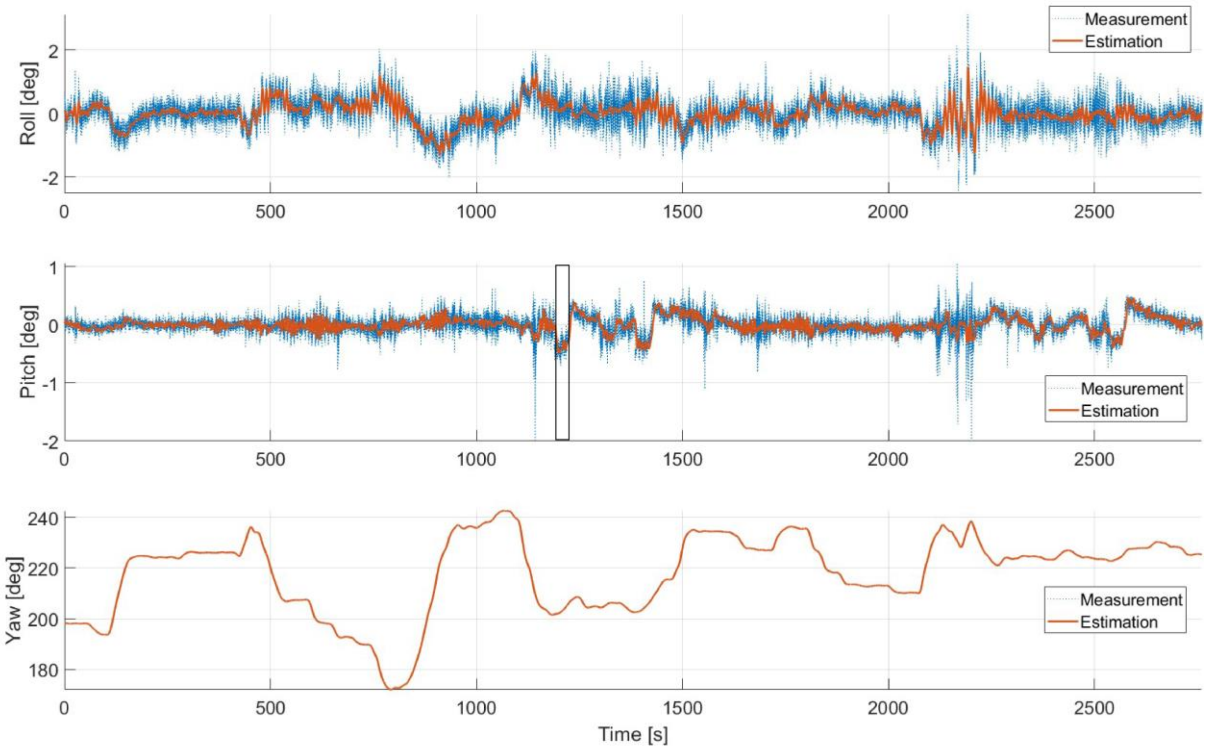

Fig. 12. Euler angle: direct 'measurements' versus results calculated from state 'estimations'.

In addition, the attitude estimate procedure based on Eqs. (20) to (24) yields more accurate angular rate and angular acceleration values than direct measurements. This is again attributed to the use of multi-channel information (i.e., both 'measurements' and physical process models) in the UKF algorithm.

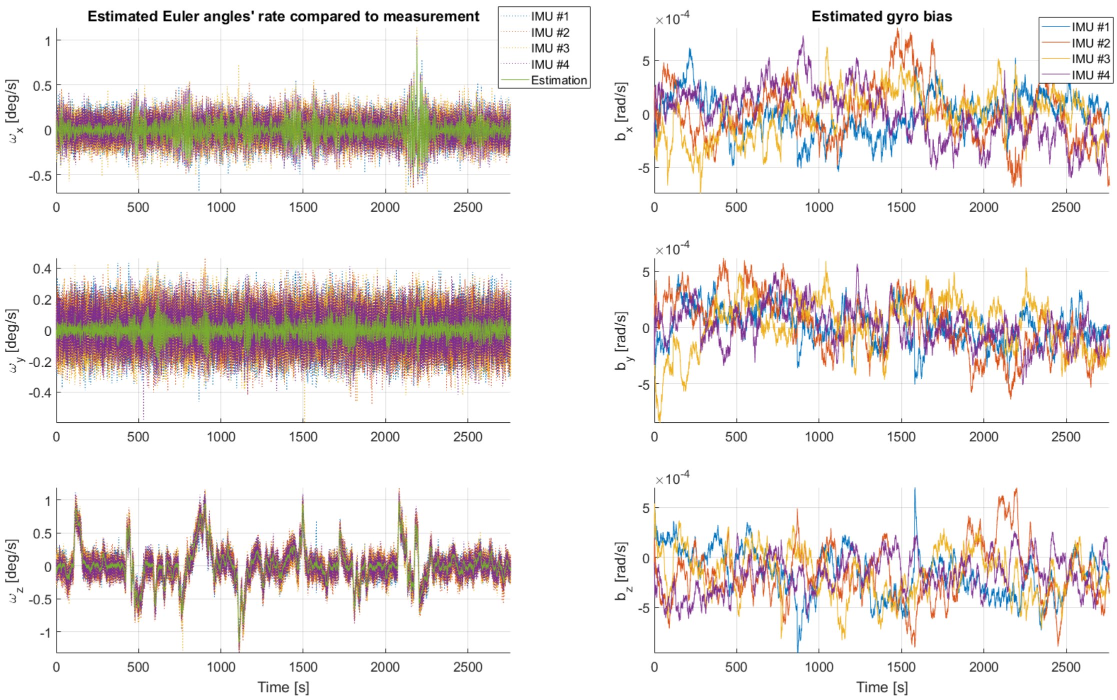

Fig. 13. Euler angular rate: direct 'measurements' versus results calculated by state 'estimation' (left column) and the associated estimation bias (right column).

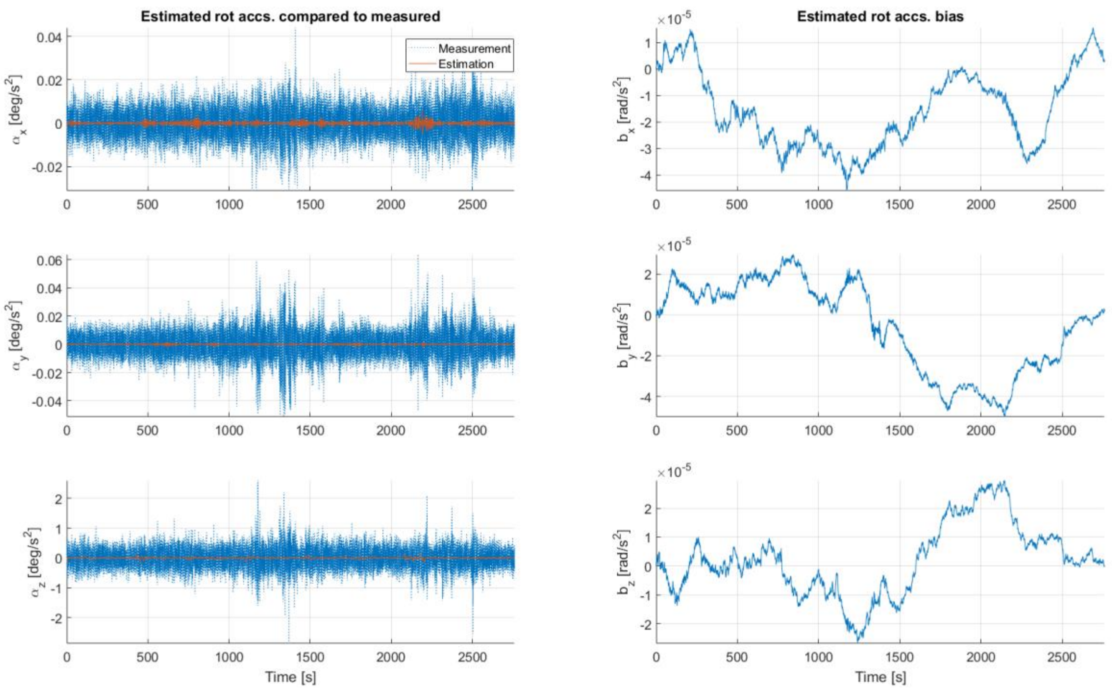

Fig. 14. Euler angle acceleration: direct 'measurements' versus results calculated via state 'estimation' (left column) and associated estimation biases (right column).

Fig. 13 and Fig. 14 present angular rate and angular acceleration measurements and state estimation results, respectively. The same effects of the attitude estimation algorithm can be observed. It is worth noting though that the ‘measurement’ of angular acceleration is in fact calculated from Eq. (12) based on measured linear acceleration and angular rates. Naturally, short-term noise in IMU measurements is passed over to the calculated angular rate. The attitude estimation procedure is again used to process angular acceleration data. According to the quantified ‘estimation bias ’ presented in the right column of Fig. 13 and Fig. 14, rather minimal bias values are achieved via attitude estimation.

5.2 Linear motion estimation

Using a similar estimation concept, the linear motion of the ship is obtained. The transit velocity of the ship is presented in Fig. 15. Extracting the velocity of a floating body is relatively easy. The most conventional approach involves taking the first time derivative of position information (see Eq. (25)). The results of this direct derivative approach used in NED are presented in the right-hand column of Fig. 15 together with estimations according to additional physical processes presented in Eqs. (26) and (27).

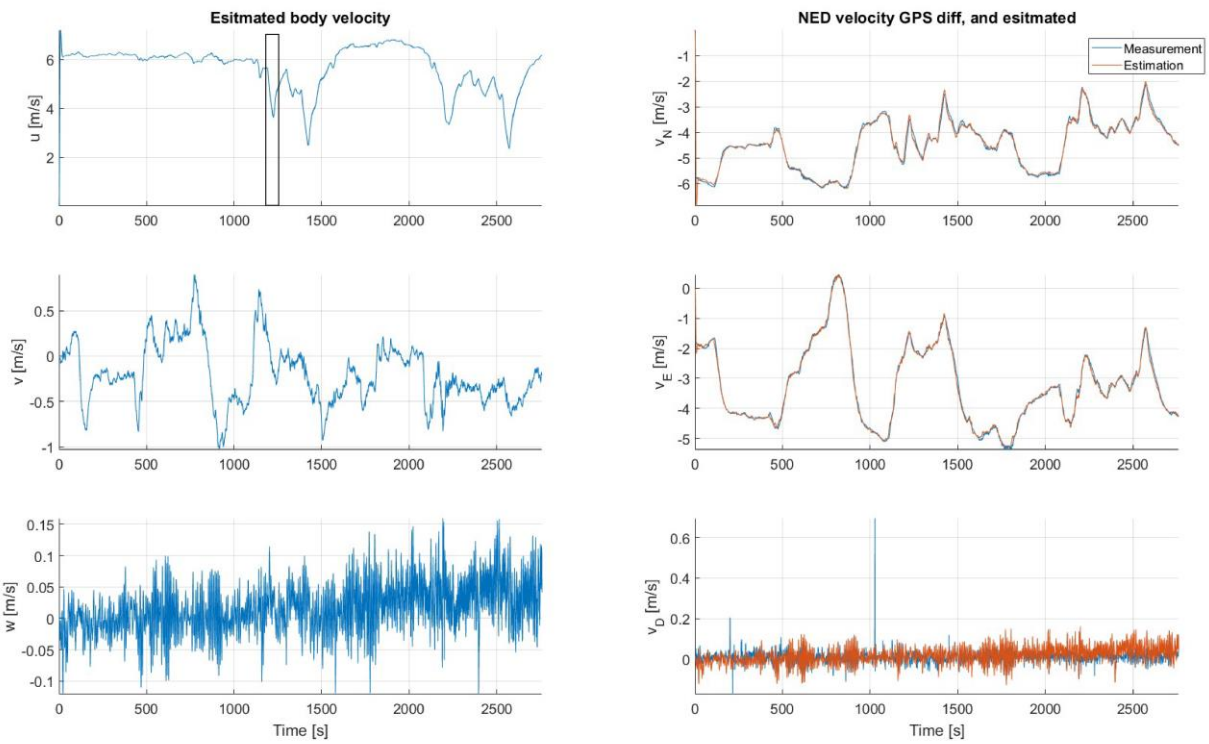

Fig. 15. Linear velocity in the body-fixed coordinate system (left column); and in NED (right column) with: direct ‘measurements’ (i.e., blue line obtained by GPS data’s time derivatives) versus calculated results by state ‘estimation’.

Minor differences between the measured and estimated velocities can be identified in the right-hand column of Fig. 15, denoting the correctness of the estimation approach described in this paper. In addition, sporadic errors magnified by time derivatives, e.g., the peak v_D observed in the 'measurement' shown in the right-hand column of Fig. 15, are removed via the estimation procedure.

The linear velocity is also presented in the body-fixed coordinate system in the left-hand column of Fig. 15, which shows a dominate velocity ($u \approx 6\,\mathrm{m/s}$) in the surge direction, whereas fewer velocity components are observed in the sway v and heave w directions. Such behaviour is in reasonable correspondence with the ship path presented in Fig. 7 for the selected time window (from 06:49:00 to 07:35:00).

When applying Eq. (1) for the current case study, an important input is linear acceleration. Fig. 16 presents linear acceleration obtained from 'measurements' and calculations obtained by state 'estimation'. Note here that the measured acceleration values are actually derived from four IMU measurement after being transformed into the CO and are calculated using Eq. (12).

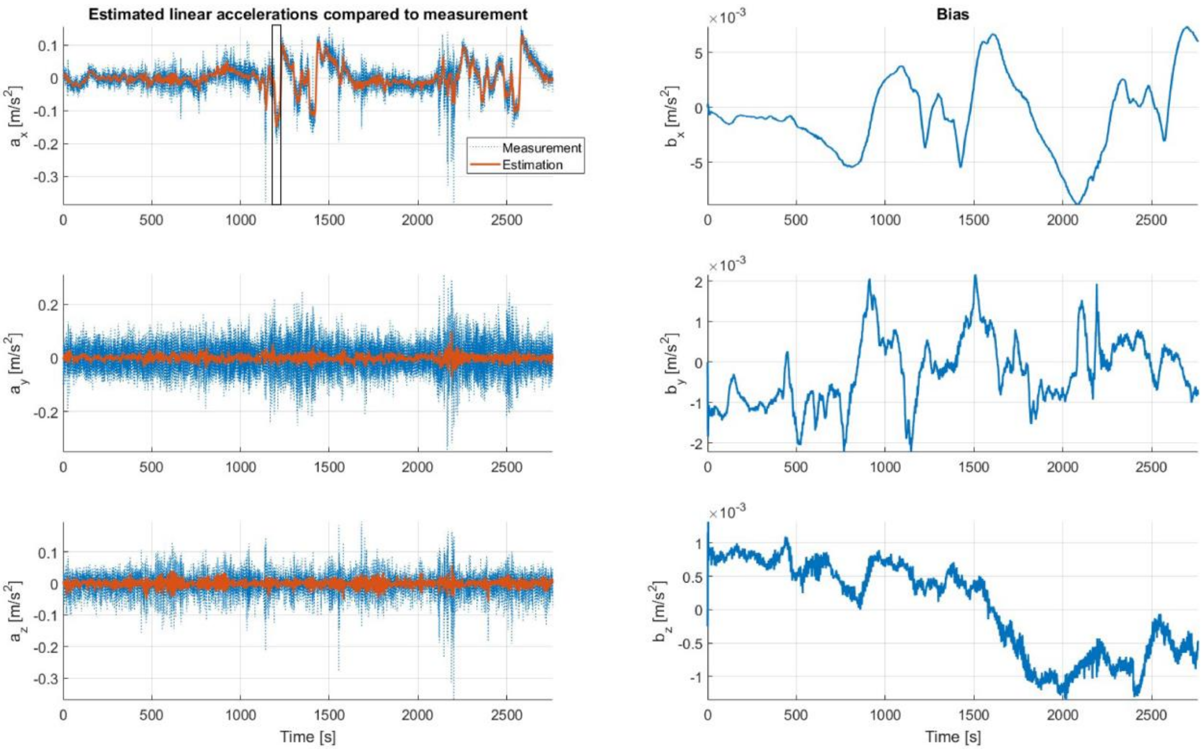

Fig. 16. Estimated linear acceleration of the body-fixed coordinate system versus measurements.

In discussing the results it is informative to correlate the estimated linear acceleration values shown in Fig. 16 with the estimated linear velocity shown in Fig. 15. For example, as Fig. 15 shows, within the time period of [1188 s, 1228 s], the surge velocity (bounded in a black box) is decreasing. This is reflected in Fig. 16, in which (also shown in the bounded black box) negative surge acceleration is measured/estimated. A similar correlation is shown in Fig. 12, in which for the same time window the ship is pitching down (negative pitch angle) as is decelerating. This example shows that different components of the developed algorithm, the attitude and linear motion estimation, are fully coupled, generating reasonable and synchronised results.

Such coupling is rather important as demonstrated by the importance of gravity compensation in Fig. 17. As described above, the accuracy of linear acceleration a is dependent on angular information Θ due to the use of the gravity compensation procedure (see Eqs. (15)). For the current case study this is illustrated in Fig. 17.

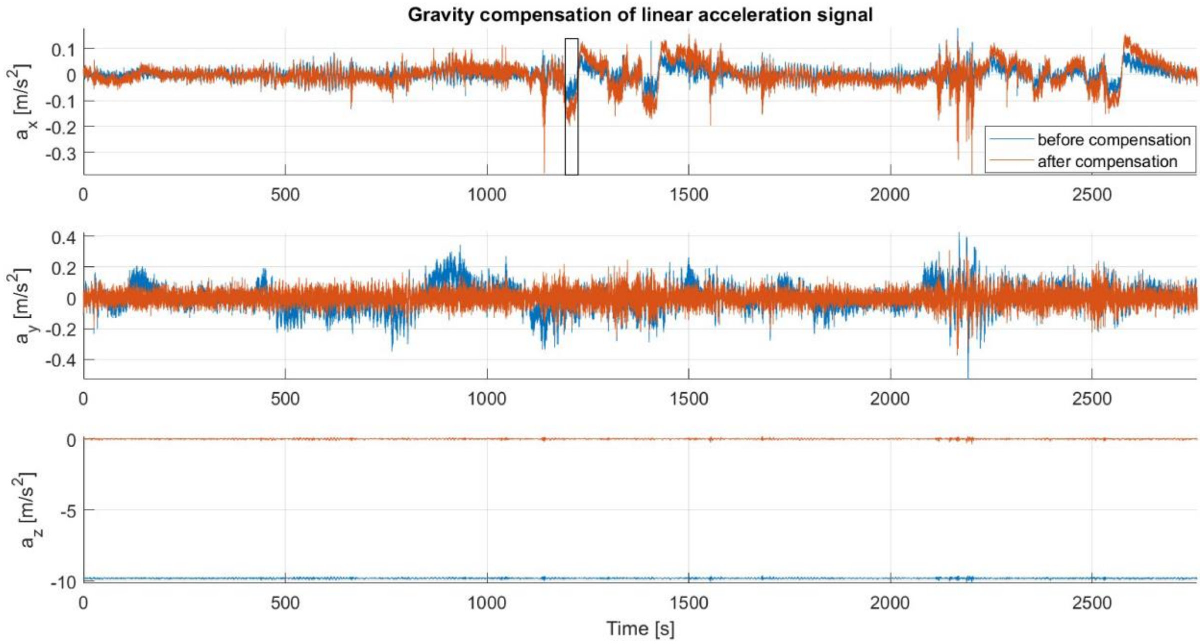

Fig. 17. The effect of gravity compensation on linear acceleration.

As an example, during the same deceleration period (i.e., from 1188 s to 1228 s) the ship is pitching down (i.e., negative pitch angle θ), the measured deceleration magnitude $\left|a_x^m\right|$ in the surge direction can be written in Eq. (45) as shown in Fig. 18a.

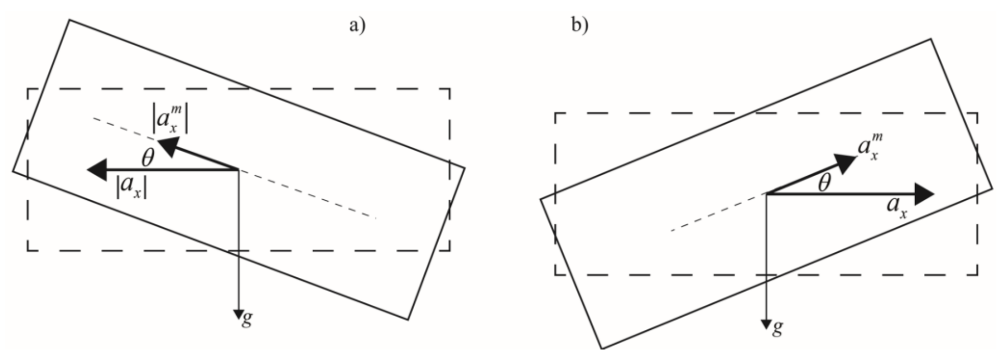

Fig. 18. 2-DoF example of gravity compensation in the surge direction for pitch in a) deceleration and b) acceleration conditions.

$$\left|a_x^m\right| = \left|a_x\right| \cos\left|\theta\right| - g \sin\left|\theta\right| \;\rightarrow \left|a_x\right| = \left(\left|a_x^m\right| + g \sin\left|\theta\right|\right) / \cos\left|\theta\right| \;\rightarrow \left|a_x\right| \geq \left|a_x^m\right| \tag{44}$$

The results presented in Eq. (44) show that after gravity compensation, the magnitude of actual surge acceleration $|a_x|$ is larger than what is measured by the IMUs before compensation $|a_x^m|$. This trend is illustrated by the bounded black box shown in Fig. 17 (i.e., $a_x < a_x^m < 0$). Similarly, for the consequent acceleration period, the measured acceleration a_x^m (now positive) can be written in Eq. (46) according to Fig. 18. The magnitude of actual surge acceleration a_x is greater than it is before compensation a_x^m (also positive). This behaviour is also reflected in Fig. 17 immediately after the bounded black box (i.e., $a_x > a_x^m > 0$).

$$a_x^m = a_x \cos|\theta| - g \sin|\theta| \;\rightarrow\; a_x = (a_x^m + g \sin|\theta|) / \cos|\theta| \;\rightarrow\; a_x \geq a_x^m \tag{45}$$

This simple exercise quantitatively shows the importance of gravity compensation to linear acceleration and especially when high levels of angular displacement are encountered.

5.3 Load component calculations

From the satisfactory motion estimations presented in the above sections we present our load component calculations in this section. Flow velocities u_p passing through the propeller are plotted in Fig. 19 with reference to the ship's surge velocity. Fig. 19 shows that during much of the transit period for the selected case, the propeller's flow velocity is rather constant in agreement with the ship's relatively constant surge velocity. Moreover, Fig. 19 illustrates that with Oden's deceleration during transit, e.g., during the time window of 1188 s to 1228 s, a negative flow velocity is found. This means that Oden's propellers were rotating in reverse and that the ship was attempting to slow down.

The flow velocity u_p passing through the propeller is correlated with the flow velocity u_r passing through the rudder in Eq. (34). Thus, using the propulsion calculation model introduced in Section 3.4, the propulsion force history τ_p can be calculated. According to Fig. 19 this force component remains positive for the majority of the time whereas negative cases are encountered during the ship's deceleration. In this regard we present in Fig. 20 the calculated load components' history for this case study. In Fig. 20, τ_p stabilises roughly 1400 kN for the majority of the transit time whereas negative values were found during deceleration. This is in agreement with our expectations based on the flow velocity history shown in Fig. 19. We in turn examine each load component's calculation in greater detail.

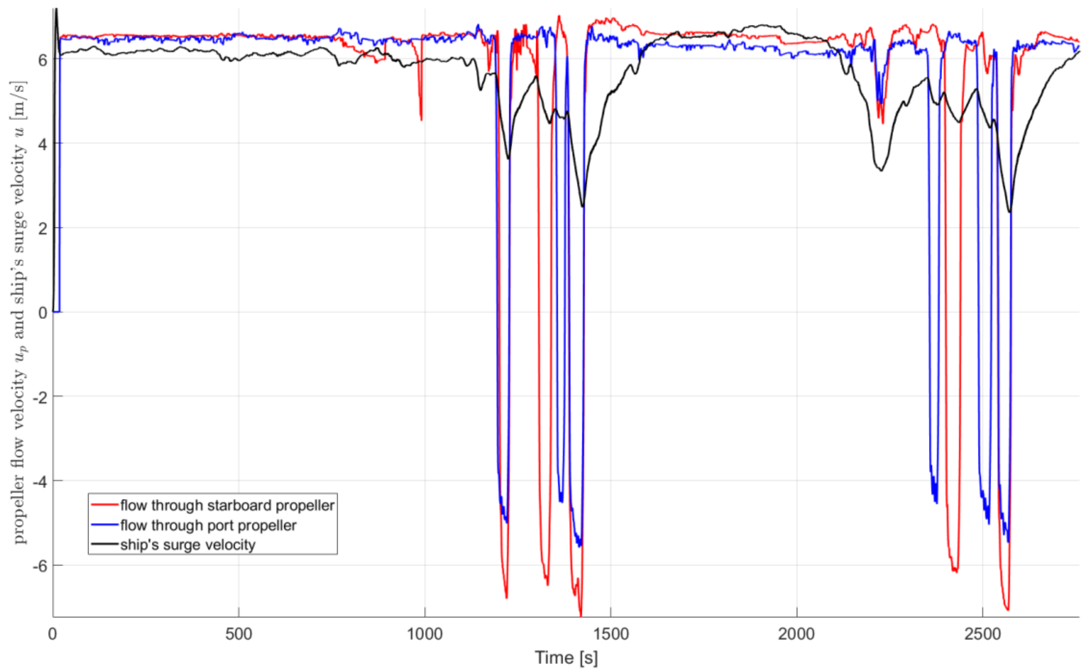

Fig. 19. Ship velocity in the surge direction versus the flow velocity passing through the propellers.

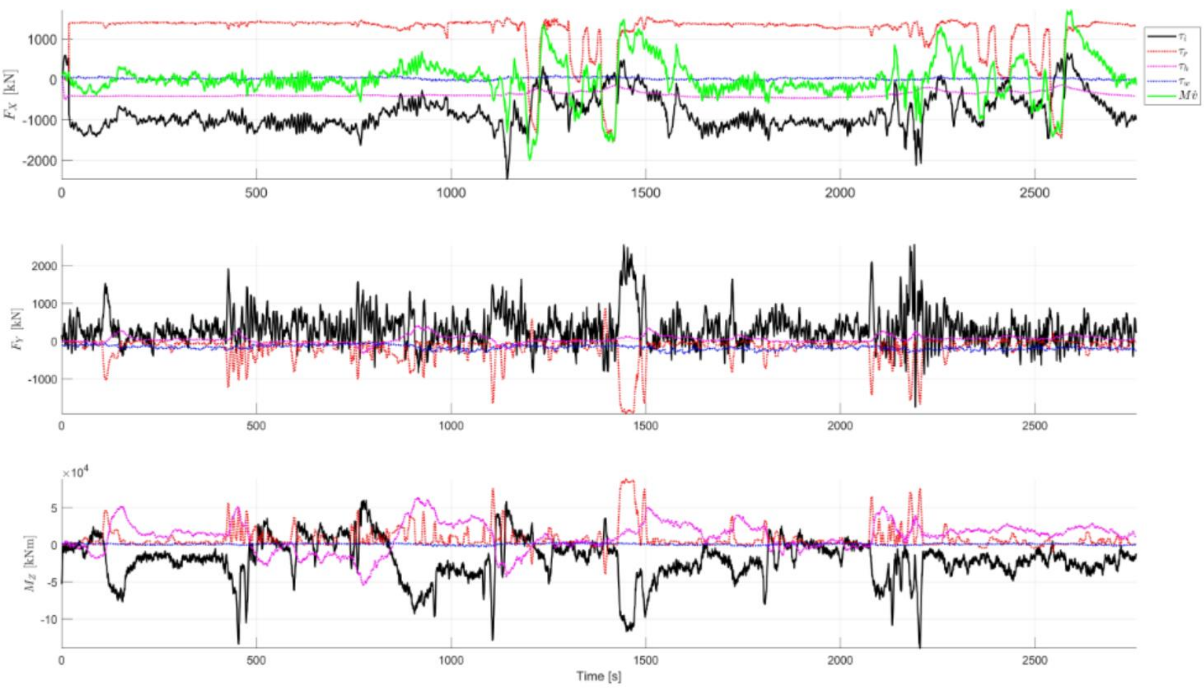

Fig. 20. Different calculated load components histories for the surge, sway and yaw directions.

Regarding hydrodynamic forces τ_h, aside from ship geometries they are purely dependent on the ship's linear and angular velocities according to formulations shown in Eq. (36). As shown in the left-hand column of Fig. 15, the ship always maintains a positive surge velocity, meaning that the hydrodynamic force is always acting against the ship's surge motion as a form of resistance (i.e., τ_h is always negative in the surge direction). This qualitative expectation is reflected in Fig. 20, in which, τ_h maintains a negative value of roughly -400 kN during transit.

In terms of wind resistance we first plot the wind rose with reference to the ship's surge direction in Fig. 21, from which we find that the prevailing wind facilitates Oden's transit in the positive surge direction. Furthermore, Fig. 21 shows that a negative wind force in the sway direction is expected. These two qualitative observations based on the wind rose are substantiated by results shown in Fig. 20, in which a positive wind force toward the surge direction at roughly 10 kN and a negative wind force in the sway direction with a magnitude of roughly 100 kN are shown. τ_w generally accounts for a small portion of the considered load components.

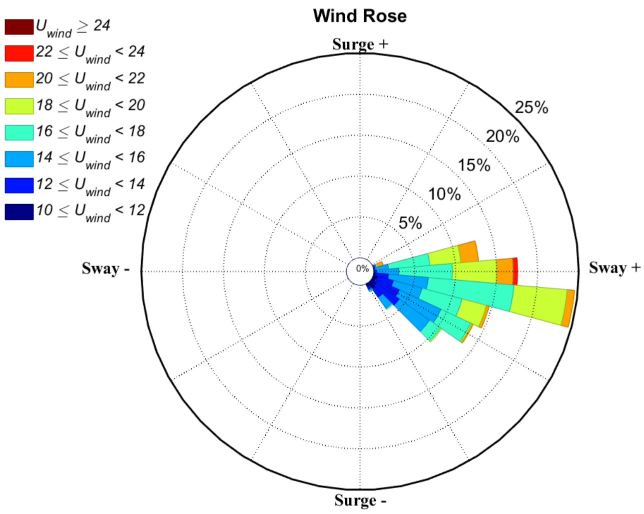

Fig. 21. Relative wind speeds and directions measured during Oden's transit for the selected time window.

With force components (τ_p , τ_h, τ_w and inertia $M\dot{V}$) calculated, the ice load history τ_i can be back-calculated according to Eq. (1). In the next section this indirectly calculated ice load is compared to one existing semi-theoretical and semi-empirical formula in predicting managed ice loads.

5.4 Ice load comparison

According to Palmer and Croasdale (2013), managed ice loads can be calculated from Eq. (47) with parameters fitted to field data drawn from Kulluk (Wright, 1999).

$$F_X = \sigma Bh(1+\frac{\mu}{\tan\beta})+\frac{cBh}{\tan\beta}+2Lh(\mu\sigma+c) \tag{46}$$

In Eq. (46),

σ , c — are the ambient ice pressure and ice field cohesion, respectively. For the selected transit case, little pressure accumulated within the ice. According to recommendations made by Palmer and Croasdale (2013), $\sigma = 4\,\text{kPa}$ and $c = 2\,\text{kPa}$;

μ — is the ice-ice friction coefficient and is designated as 0.1 in this study;

β — is the angle of potential ice accumulation measured at the ship bow. According to recommendations made by Palmer and Croasdale (2013), we use $\beta = 15^{\circ}$;

B , L_{oa} — are the ship beam width (25 m) and length (108 m), respectively;

h — is ice thickness.

Most of the inputs used in Eq. (46) were specifically recommended by Palmer and Croasdale (2013) in their original study. The only parameter presenting uncertainty is ice thickness h . During the expedition, we continuously measured ice thicknesses using an Electronic-Magnetic (EM) device and a video camera (Lu et al., 2016b). We do not have ice thickness information for the return journey (i.e., Sep 30th), as all of the equipment was gradually dismantled. However, we have rather satisfactory ice thickness information for the previous days; and it ranges from 0.7 to 1.2 m (Lubbad et al., 2016). This provides us with an averaged ice thickness of roughly 0.95 m. Specifically, the measured ice thickness history for Sep 29th is shown in Fig. 22 (echoing ice conditions observed during the return journey), revealing an averaged ice thickness of 0.9 m.

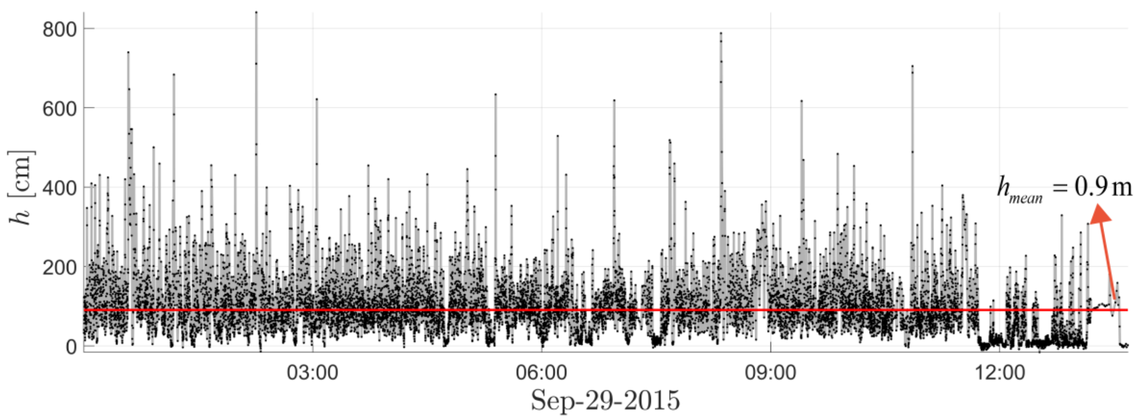

Fig. 22. Measured ice thickness history for the previous day (i.e., Sep 29th, 2015).

With the above inputs and presumed reasonable ice thickness of $h = 0.9\,\mathrm{m}$ we calculate the managed ice load $F_X = 769.91\,\mathrm{kN}$ illustrated with a red line in Fig. 23. Similarly, we take the average $\left|\bar{F}_X\right| = 821.89\,\mathrm{kN}$ of the estimated ice load of the surge direction from Fig. 20 and plot it as a blue line in Fig. 23. We can see that the averaged ice loads obtained from these two different approaches are quite comparable with an error of 8%. However, the algorithm proposed in this paper offers us full ice load histories as opposed to Eq. (46). Moreover, we used the lower and upper values of ice thickness, i.e., 0.7 to 1.2 m, and repeated the above calculations. The averaged ice resistance $\left|\bar{F}_X\right| = 821.89\,\mathrm{kN}$ falls well within the range shown in Fig. 23.

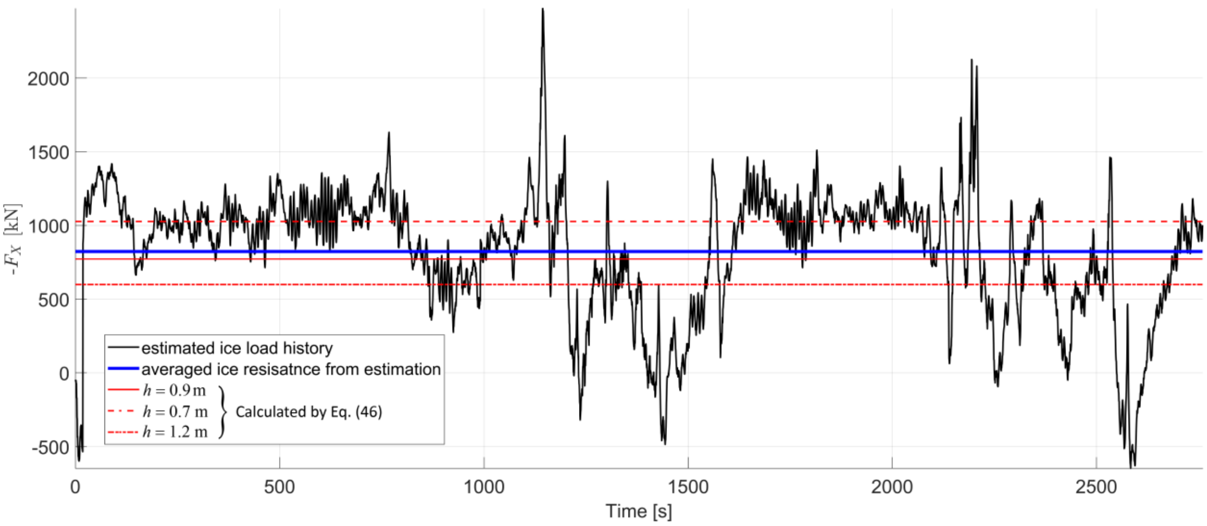

Fig. 23. Comparisons of the identified ice load history and semi-empirical and semi-analytical formula calculations.

The above comparison is encouraging, although only the average ice load is compared. Considering the non-invasive installation of IMUs (see Fig. 9), the algorithm proposed in this paper is capable of effectively extracting ice load histories presenting satisfactory ice load levels during interactions between ice and floating structures. Moreover, the ($\approx 2800\,\mathrm{s}$) calculation shown in Fig. 20 takes only roughly 100 s to complete using a normal personal laptop. This demonstrates the potential of the proposed model to make real-time ice load estimations in the field.

However, the approximation nature of Eq. (46) in the preceding comparison should be cautioned. The derivation of Eq. (46) is based on an assumption that rather small ice floes constitute to an entire ice field and that data fit from another type of structure, i.e., Kulluk (Croasdale et al., 2009). As Fig. 6 shows, ice conditions that Oden was exposed to in our case study was not filled with small ice floes. However, those ice floes are not large enough that the fractures of sea ice start to dominate the physical process (Lu et al., 2015a; Lu et al., 2015b; Lu et al., 2016a). The main physical processes contributing to the major ice resistance are still rearranging surrounding ice floes and its associated friction. These processes can be largely approximated from Eq. (46), thereby substantiating results obtained from the algorithm proposed in this paper.

Nevertheless, the proposed algorithm can be improved further. Our original ice load calculation was conducted by calculating different load components (hydrodynamic forces, propulsion and wind forces) using well-established methods. The accuracy of these force components are susceptible to the accuracy of input value measurements and to corresponding calculation methods. For example, as the anonymous reviewer pointed out, these different load components were of different time scales and a ‘proper’ processing of these load components is needed to further increase the reliability of the proposed algorithm. The use of more mature models and/or of more inputs for these load components may increase accuracy levels. Moreover, the accuracy and stability of IMUs can always be improved to improve the accuracy of the algorithm proposed in this paper.

6 Conclusions

Given the scarcity and importance of field global ice load measurements and given difficulties associated with measuring ice loads directly with conventional methods, this paper proposes an algorithm based on four Inertial Measurement Units (IMUs) non-invasively installed onto a floating structure to estimate the structure’s motion in real-time. In using structural motion information and relatively mature models to calculate other force components for a floating structure positioned in ice, e.g., hydrodynamic forces, propulsion, and wind forces, the algorithm managed to effectively yield global ice resistance values.

A case study of the Oden icebreaker’s transit through the Marginal Ice Zone was conducted using the proposed algorithm. Reasonable and synchronised ship motion data and various load component histories were obtained. In particular, the estimated ice load was compared to existing semi-theoretical and semi-empirical managed ice load formula predictions, and only small errors were found from comparisons of mean force levels. This proves the proposed algorithm’s capacity to yield reasonable ice load results. The proposed algorithm can yield global ice load histories, which are of value for various ice engineering applications. Moreover, in the case study an roughly 2800 s (roughly 45 min) ship transit scenario was examined using the proposed algorithm within 100 s to yield all necessary information. These are the ship’s movements and different load components experienced during transit. We thus demonstrate the algorithm’s potential to make real-time global ice load estimations in the field.

Acknowledgements

The Oden Arctic Technology Research Cruise 2015 (OATRC2015) was supported by the ExxonMobil Upstream Research Company and was performed by the Norwegian University of Science and Technology (NTNU) in cooperation with the Swedish Polar Research Secretariat (SPRS) and the Swedish Maritime Administration (SMA). Special thanks are given to the crew of the Oden and Frej icebreakers. The authors are also grateful for valuable discussions held with Dr. Andrei Tsarau, Mr. Hongtao Li and Mr. Hans-Martin Heyn and for constructive suggestions given by Dr. Raed Lubbad, who was also actively involved in organizing the research expedition.

References

ABS, 2011. Guide for Ice Loads Monitoring Systems, American Bureau of Shipping, Houston, TX 77060 USA.

Buhmann, A., Peters, C., Cornils, M. and Manoli, Y., 2006. A GPS aided full linear accelerometer based gyroscope-free navigation system, Position, Location, And Navigation Symposium, 2006 IEEE/ION. IEEE, pp. 622-629.

Croasdale, K.R., Bruce, J.R. and Liferov, P., 2009. Sea ice loads due to managed ice, Proceedings of the 20th International Conference on Port and Ocean Engineering under Arctic Conditions (POAC'09), Luleå, Sweden, pp. 139.

Danielewicz, B.W., Metge, M. and Dunwoody, A.B., 1983. On estimating large scale ice forces from deceleration of ice floes, The seventh international conference on port and ocean engineering under arctic conditions, Espoo, pp. 537-546.

Dolgopolov, Y., Afanasiev, V., Koren'Kov, V. and Panfilov, D., 1975. Effect of hummocked ice on the piers of marine hydraulic structures, International Symposium on Ice Problems, 3rd, Proceedings, Dartmouth College, Hanover, NH. Aug., 18-21. 1975.

Faltinsen, O.M., 1993. Sea loads on ships and offshore structures, 1. Cambridge Univ Pr.

Fossen, T.I., 2011a. Environmental Forces and Moments, Handbook of Marine Craft Hydrodynamics and Motion Control. John Wiley & Sons, Ltd, pp. 187-225.

Fossen, T.I., 2011b. Front Matter, Handbook of Marine Craft Hydrodynamics and Motion Control. John Wiley & Sons, Ltd, pp. i-xix.

Fossen, T.I., 2011c. Kinematics, Handbook of Marine Craft Hydrodynamics and Motion Control. John Wiley & Sons, Ltd, pp. 15-44.

Fossen, T.I., 2011d. Maneuvering Theory, Handbook of Marine Craft Hydrodynamics and Motion Control. John Wiley & Sons, Ltd, pp. 109-132.

Fossen, T.I., 2011e. Models for Ships, Offshore Structures and Underwater Vehicles, Handbook of Marine Craft Hydrodynamics and Motion Control. John Wiley & Sons, Ltd, pp. 133-186.

Fossen, T.I., 2011f. Sensor and Navigation Systems, Handbook of Marine Craft Hydrodynamics and Motion Control. John Wiley & Sons, Ltd, pp. 285-342.

Frederking, R.M.W., 2005. Local Ice Pressures on the ODEN 1991 Polar Voyage, Proceedings 18th International Conference on Port and Ocean Engineering under Arctic Conditions, POAC'05, pp. 353-363.

Haas, C. and Jochmann, P., 2003. Continuous EM and ULS thickness profiling in support of ice force measurements, Proceedings of the 17th International Conference on Port and Ocean Engineering under Arctic Conditions, Trondheim, Norway, pp. 849 - 856.

ISO/FDIS/19906, 2010. Petroleum and natural gas industries - Arctic offshore structures,International Standard, International Standardization organization, Geneva, Switzerland,.

Johnston, M., Ritch, R. and Gagnon, R., 2008a. Comparison of impact forces measured by different instrumentation systems on the CCGS Terry Fox during the Bergy Bit Trials. Cold Regions Science and Technology, 52(1): 83-97.

Johnston, M., Timco, G.W., Frederking, R. and Miles, M., 2008b. Measuring global impact forces on the CCGS Terry Fox with an inertial measurement system called MOTAN. Cold Regions Science and Technology, 52(1): 67-82.

Julier, S.J. and Uhlmann, J.K., 2004. Unscented filtering and nonlinear estimation. Proceedings of the IEEE, 92(3): 401-422.

Kjerstad, Ø.K. and Skjetne, R., 2016. Disturbance Rejection by Acceleration Feedforward for Marine Surface Vessels. IEEE Access, 4: 2656-2669.

Lensu, M. and Hänninen, S., 2003. Short term monitoring of ice loads experienced by ships, Proceedings of the International Conference on Port and Ocean Engineering Under Arctic Conditions.

Leppäranta, M., 2011. The drift of sea ice. Springer, Helsinki.

Lindegaard, K.-P., 2003. Acceleration feedback in dynamic positioning.

Lindqvist, G., 1989. A straightforward method for calculation of ice resistance of ships, Proceedings of POAC 1989, pp. 722-735.

Lu, P. and Li, Z., 2010. A Method of Obtaining Ice Concentration and Floe Size From Shipboard Oblique Sea Ice Images. Geoscience and Remote Sensing, IEEE Transactions on, 48(7): 2771-2780.

Lu, P., Li, Z.J., Zhang, Z.H. and Dong, X.L., 2008. Aerial observations of floe size distribution in the marginal ice zone of summer Prydz Bay. Journal of Geophysical Research: Oceans, 113(C2): n/a-n/a.

Lu, W., Heyn, H.-M., Lubbad, R. and Løset, S., 2018. A large scale simulation of floe-ice fractures and validation against full-scale scenario. International Journal of Naval Architecture and Ocean Engineering.

Lu, W., Lubbad, R. and Løset, S., 2014. Simulating Ice-Sloping Structure Interactions With the Cohesive Element Method. Journal of Offshore Mechanics and Arctic Engineering, 136(3): 031501-031501.

Lu, W., Lubbad, R. and Løset, S., 2015a. In-plane fracture of an ice floe: A theoretical study on the splitting failure mode. Cold Regions Science and Technology, 110(0): 77-101.

Lu, W., Lubbad, R. and Løset, S., 2015b. Out-of-plane failure of an ice floe: Radial-crack-initiation-controlled fracture. Cold Regions Science and Technology, 119: 183-203.

Lu, W., Lubbad, R., Løset, S. and Kashafutdinov, M., 2016a. Fracture of an ice floe: Local out-of-plane flexural failures versus global in-plane splitting failure. Cold Regions Science and Technology, 123: 1-13.

Lu, W., Zhang, Q., Lubbad, R., Løset, S. and Skjetne, R., 2016b. A Shipborne Measurement System to Acquire Sea Ice Thickness and Concentration at Engineering Scale, Arctic Technology Conference 2016, St. John's, Newfoundland and Labrador.

Lubbad, R., Løset, S., Hedman, U., Holub, C. and Matskevitch, D., 2016. Oden Arctic Technology Research Cruise 2015, Proc. of the Arctic Technology Conference (ATC), St. Johns's, Newfoundland and Labardor, Canada.

Lubbad, R., Løset, S., Lu, W., Tsarau, A. and Van den Berg, M., submitted in 2017. An overview of the Oden Arctic Technology Research Cruise 2015 (OATRC2015) and numerical simulations performed with SAMS driven by data collected during the cruise. Cold Regions Science and Technology.

Lubbad, R., Løset, S. and Skjetne, R., 2015. Numerical Simulations Verifying Arctic Offshore Field Activities, Proceedings of the International Conference on Port and Ocean Engineering Under Arctic Conditions, Trondheim, Norway.

Metrikin, I., Gürtner, A., Bonnemaire, B., Tan, X., Fredriksen, A. and Sapelnikov, D., 2015. SIBIS: A Numerical Environment for Simulating Offshore Operations in Discontinuous Ice, Proceedings of the International Conference on Port and Ocean Engineering Under Arctic Conditions.

Molland, A.F., Turnock, S.R. and Hudson, D.A., 2017. Ship resistance and propulsion. Cambridge university press.

Noureldin, A., Karamat, T.B. and Georgy, J., 2012. Fundamentals of inertial navigation, satellite-based positioning and their integration. Springer Science & Business Media.

Nyseth, H., Frederking, R. and Sand, B., 2013. Evaluation of global ice load impacts based on real-time monitoring of ship motions, Proceedings of the International Conference on Port and Ocean Engineering Under Arctic Conditions.

Palmer, A.C. and Croasdale, K.R., 2013. Arctic Offshore Engineering. World Scientific.

Perez, T., 2006. Ship motion control: course keeping and roll stabilisation using rudder and fins. Springer Science & Business Media.

Ritch, R., Frederking, R., Johnston, M., Browne, R. and Ralph, F., 2008. Local ice pressures measured on a strain gauge panel during the CCGS Terry Fox bergy bit impact study. Cold Regions Science and Technology, 52(1): 29-49.

Sanderson, T.J.O., 1988. Ice mechanics and risks to offshore structures.

Sayed, M., Kubat, I., Watson, D., Wright, B., Gash, R. and Millan, J., 2015. Simulations of the StationKeeping of Drillships Under Changing Direction of Ice Movement. Offshore Technology Conference.

Sørensen, A.J., 2012. Marine control systems propulsion and motion control of ships and ocean structures lecture notes.

Tan, C.-W. and Park, S., 2005. Design of accelerometer-based inertial navigation systems. IEEE Transactions on Instrumentation and Measurement, 54(6): 2520-2530.

Timco, G.W., 2011. Isolated ice floe impacts. Cold Regions Science and Technology, 68(1): 35-48.

Titterton, D. and Weston, J.L., 2004. Strapdown inertial navigation technology, 17. IET.

Tsarau, A., Løset, S. and Grindstad, T., 2014. Propeller wash by an icebreaker, 22nd IAHR International Symposium on Ice Singapore.

Wright, B., 1999. Evaluation of full scale data for moored vessel stationkeeping in pack ice. PERD/CHC Report: 26-200.

Zappa, B., Legnani, G., Van Den Bogert, A.J. and Adamini, R., 2001. On the number and placement of accelerometers for angular velocity and acceleration determination. TRANSACTIONS-AMERICAN SOCIETY OF MECHANICAL ENGINEERS JOURNAL OF DYNAMIC SYSTEMS MEASUREMENT AND CONTROL, 123(3): 552-553.